

University of Trento

Sara Roccabianca

**MULTILAYERED STRUCTURES UNDER
LARGE BENDING: FINITE SOLUTION AND
BIFURCATION ANALYSIS**

Prof. Davide Bigoni (Tutor)

Prof. Massimiliano Gei (Co-Tutor)

UNIVERSITY OF TRENTO

Engineering of Civil and Mechanical Structural Systems, Cycle XXIII

Ph.D. program Head: Davide Bigoni

Final Examination: 25/03/2011

Board of Examiners

Prof. Roberto Oboe (Università degli Studi di Padova)

Prof. Robert McMeeking (University of California)

Prof. Ettore Pennestri (Università degli Studi di Roma)

Prof. Antonio DeSimone (SISSA - Scuola Internazionale Superiore di Studi
Avanzati)

Abstract

Finite plane strain bending is solved for a multilayered elastic–incompressible thick plate. This multilayered solution, previously considered only in the case of homogeneity, is in itself interesting and reveals complex stress states such as the existence of more than one neutral axis for certain geometries. The bending solution is employed to investigate possible in-plane and out-of-plane incremental bifurcations. The analysis reveals that a multilayered structure can behave in a completely different way from the corresponding homogeneous plate. For a thick plate of neo-Hookean material for instance, the presence of a stiff coating strongly affects the bifurcation critical angle. Experiments designed and performed to substantiate our theoretical findings demonstrate that the theory can be effectively used as a design tool for predicting the capability of an elastic multilayered structure.

Contents

1	Introduction	7
2	Notation and governing equations	15
3	Finite bending of a layered block	19
3.1	Kinematics	19
3.2	Stress	23
3.3	Examples of multilayered plates under finite bending	25
4	In-plane incremental bifurcations	29
4.1	General formulation	29
4.2	Bifurcation of a bilayer	34
5	Numerical procedures	47
5.1	The determinantal method	47
5.2	The compound matrix method for a bilayer	50
6	Experiments on rubber blocks	57
7	Out-of-plane incremental bifurcations	67
7.1	General formulation	67
7.2	Examples	74
7.2.1	The homogeneous block	74
7.2.2	A bilayered block	76

CONTENTS

8	Conclusions	83
A	Matrices of numerical methods	85
	References	89

1

Introduction

Natural (geological formations, biological materials) and man-made (sandwich panels, submarine coatings, microelectronic devices) structures are often made up of layers of different materials glued together, the so-called ‘multilayers’. The possibility of achieving large deformations in these structures is limited by the occurrence of various forms of bifurcations. For instance, compressive strain is limited by buckling and subsequent folding (see the example reported in Fig. 1.1 on the left), uniform tensile strain may terminate with shear band formation and growth, while uniform flexure may lead to the formation of bifurcation modes such as undulations and creases (see the example reported in Fig. 1.1 on the centre and right). Bifurcation is therefore an important factor in the design of multilayered materials, so that this has been the focus of a thorough research effort, which was initiated by Maurice A. Biot, Ref. [11], and continued by many others. In particular, elastic layered structures deformed in plane strain and subject to a uniform state of stress have been analyzed by Dorris and Nemat-Nasser, Steif, Papamichos et al., Dowaikh and Ogden, Benallal et al., Triantafyllidis and Lehner, Triantafyllidis and Leroy, Shield et al., Ogden and Sotiropoulos and Steigmann and Ogden, Refs. [5, 20, 21, 40, 41, 45–50, 53, 54], on the basis of the bifurcation problem of an isolated layer subject to uniform

1. INTRODUCTION

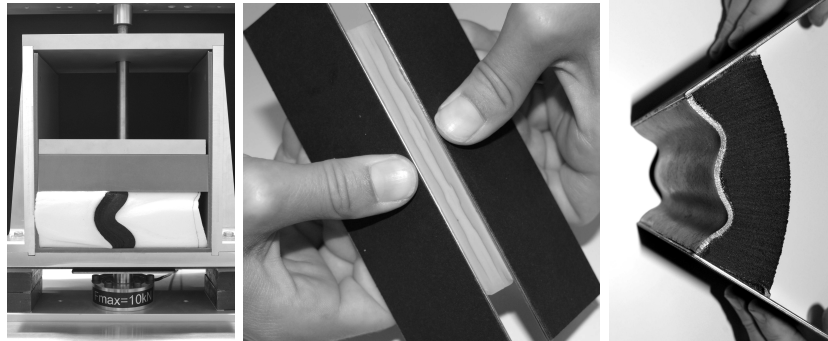


Figure 1.1: Left: a stiff (30 mm thick, neoprene) layer bonded by two compliant (100 mm thick foam) layers in a rigid wall and confined compression apparatus (note that a separation between sample and wall has occurred on the right upper edge of the sample). Centre: creases occurring at the compressive side of a rubber strip, coated at the tensile side with a 0.4 mm thick polyester transparent film, subject to flexure. Right: bifurcation of a two-layer rubber block under finite bending evidencing long-wavelength bifurcation modes (the stiff layer, made up of natural rubber, is at the compressive side of a neoprene block).

tension or compression, Refs. [30, 35, 57].

In this thesis we have generalized the solution for plane strain bending of an elastic block given by Rivlin, Ref. [42], and the subsequent analyses of incremental bifurcations, Refs. [1, 2, 12, 13, 17, 22, 52], determining the stress/strain fields during finite bending for elastic multilayers and related bifurcation analysis.

Finite bending of plates is a phenomenon common in nature and in engineered processes. Leaves are often subject to large bending for various reasons: the *pinguicola leptoceras*, curls its leaf to trap insects, the *geranium-pratensis*' pod suffers a strong bending when seeds are dispersed, and *gramineae* leaves deform into a tube to resist dehydration. Moreover, arteries unfold when cut longitudinally, on the left, thus showing that the internal stress state developed during morphogenesis is compatible with a finite bending. Bending is important in metalworking techniques and tissue-

engineered blood vessels, in which the internal fibroblast sheets are *wrapped* around a tubular support, Ref. [31]. In microelectronic devices, we may mention that flexible solar cells (made up of layers, one of which containing three-dimensional nanopillar-array photovoltaics) have a 4 mm thickness and are subject to bending up to a curvature radius of 3 cm, Ref. [23].

Although *plates suffering finite bending are often made up of layers*¹, the theory of finite elastic bending has been previously developed only under the assumption of homogeneity, Ref. [27, 34, 42, 55]. Moreover, while certain elastic multilayers can be bent until the tubular shape is reached without any appearance of inhomogeneities, crazes develop for other systems (Fig. 1.1, in the centre, and also Fig. 6.5), severely decreasing the elastic deformational capability.

Since these crazes can be interpreted as bifurcation modes localized near the surface, the bifurcation analysis becomes an important tool for design purposes. However, theoretical, Ref. [12, 13, 17, 22, 28, 52], and experimental, Ref. [26], approaches to bifurcation of plates subject to finite bending have only been considered until now under the assumption of material homogeneity. Therefore, the aims of the present thesis are:

- (i.) to provide an analytical solution to finite bending of an elastic multilayered thick plate deformed under the plane strain constraint;
- (ii.) to analyse and solve the problem of two-dimensional bifurcations possibly occurring during bending;
- (iii.) to validate our theoretical approach with experiments.

Analyzing the incremental problem we found that for several geometries and stiffness contrasts the first (‘critical’) bifurcation load corresponds to a long-wavelength mode, which results to be very close to the bifurcation

¹Leaves, arteries, and the flexible solar cells, Ref. [23], are complex structures composed of at least three layers.

1. INTRODUCTION

load associated with the surface instability limit of vanishing wavelength², a feature also common to the behaviour of a homogeneous elastic block subject to finite bending. This feature explains the experimental observation (on uniform blocks, Ref. [25, 26]) that short-wavelength modes become visible, instead of the long-wavelength modes that are predicted to occur before. Therefore, the question was left open whether or not wavelength modes longer than the short-wavelength modes available at surface instability and visible in the experiments can be experimentally displayed with a layered system in which an appropriate selection is made of stiffness and thickness contrast between layers. We provide a positive answer to this problem in this thesis, so that our calculations, based now on the compound matrix method, Ref. [4, 36–38], allow us to conclude that there are situations in which the long-wavelength modes are well-separated from the surface instability, so that systems exhibiting bifurcation modes of long wavelength can be designed. These systems have been realized by us and qualitatively tested, showing that the theory predictions are generally followed, Fig. 1.1 on the right.

The solution for finite bending of an elastic multilayer discloses the complex stress distributions that can be generated inside such structures as a result of large strains. For instance, *more than one neutral axis* may be present³ (Fig. 3.3) and weakly stressed layers may ‘bond’ a highly stressed one (Fig. 3.4). The determination of these stress states is of great importance in the design of multilayered structures, but then the question arises

² Surface instability occurs in a uniformly strained half space as a bifurcated mode of arbitrary wavelength, corresponding to a Rayleigh wave of vanishing speed. In the limit of vanishing wavelength, surface instability can be viewed as a bifurcation mode ‘adaptable’ to every boundary and state of stress of a strained body, so that it becomes a local instability mode (also called ‘failure of complementing condition’, Ref. [5]).

³ In our examples we have found situations with two (Fig. 3.2) and three (Fig. 3.3) neutral axes. More than one neutral axis can occur as induced in a multilayer by thermal loadings or residual stresses, Ref. [15, 16], in our context they occur under pure bending loading as a consequence of large strains.



Figure 1.2: Bifurcation in compression of a finely layered metamorphic rock has induced severe folding, an example of a ‘accomodation structure’ (Treadur Bay, Holyhead, N. Wales, UK; the coin in the photos is a Pound).

if such configurations can be achieved without encountering a previous bifurcation. In fact, one conclusion of the bifurcation analysis is that there is a strong difference between bifurcation loads and geometries when homogeneous structures are compared with the corresponding layered structures. For instance, a stiff and thin coating reinforcing an elastic layer strongly decreases the bifurcation bending angle of the uncoated structure, a finding fully consistent with the solutions obtained employing a surface coating model by Dryburgh and Ogden and Gei and Ogden, Ref. [22, 24]. In a bilayer, two neutral axes typically occur when a stiff layer is placed at the compressive side of the system, a case in which the differential equations become ‘numerically stiff’, so that we have employed an ‘ad hoc version’ of the compound matrix method, which is shown to allow systematic investigation of the situations in which more than one neutral axis occurs. In these cases we find a sort of ‘inversion’ of the sequence of bifurcation modes with the aspect ratio of the system, so that high-wavenumber modes are relevant for lower slender ratios than small-wavenumber modes.

Experimentally, bifurcations of homogeneous elastic strips subject to

1. INTRODUCTION

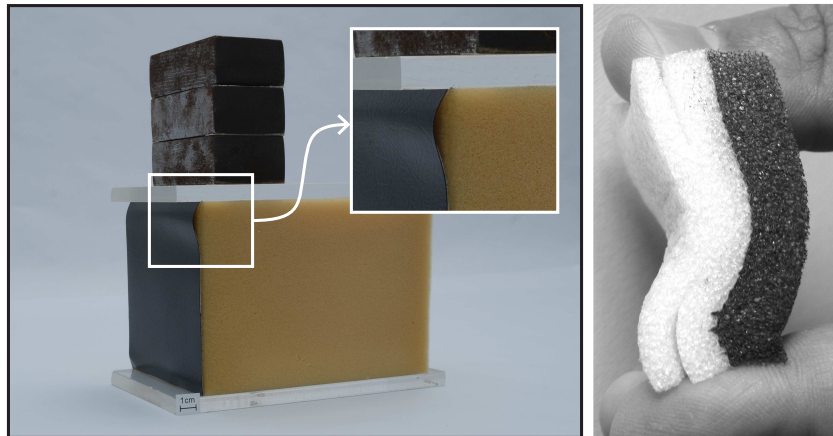


Figure 1.3: Bifurcation in compression with detachment of layers: a stiff (1 mm thick) plastic coating is detached from a foam substrate to which it was initially glued (left), three layers of foam fold with detachment, clearly visible near the edges of the sample (right).

bending have been investigated only by Gent and Cho, Ref. [26], although the experimental setting is not particularly complex. To extend their analyses to the case of layered plates, we have designed a simple device to impose a bending angle to elastic strips on which bifurcations in the form of crazes can be detected by direct visual inspection.

The bifurcation loads and modes are strongly sensible to the bonding conditions between the layers, which may be perfect (as in the case of the rock shown in Fig. 1.2), but often they may involve the possibility of slip and detachments, the so-called ‘delaminations’ (as in the cases shown in Figs. 1.3).

A simple way to account for this crucial behaviour is to introduce interfacial laws at the contact between layers. The simplest model of these laws is linear and can be formulated assuming the interface having null, Refs. [7, 9, 51], or finite (Refs. [6, 8, 14]) thickness. We will limit our attention to zero-thickness linear interfaces, across which the nominal traction increments remain continuous, but linearly related to the jump in displace-

ments, that are unrestricted. For simplicity, the materials forming the multilayer are assumed hyperelastic and incompressible, according to the general framework laid by Biot, Ref. [11], in which Mooney-Rivlin and Ogden materials, Ref. [39], as well as the J_2 -deformation theory of plasticity, are particular cases. All the material in this thesis has been published in two articles, see Refs. [10, 43, 44].

1. INTRODUCTION

2

Notation and governing equations

The notation employed throughout the present thesis and the main equations governing equilibrium in finite and incremental elasticity are now briefly recalled. Let \boldsymbol{x}^0 denote the position of a material point in some stress-free reference configuration B_0 of an elastic body. A deformation $\boldsymbol{\xi}$ is applied, mapping points of B_0 to those of the current configuration B indicated by $\boldsymbol{x} = \boldsymbol{\xi}(\boldsymbol{x}^0)$. We identify its deformation gradient by \boldsymbol{F} , *i.e.*, $\boldsymbol{F} = \text{Grad}\boldsymbol{\xi}$, and we define the right, \boldsymbol{C} , and the left, \boldsymbol{B} , Cauchy-Green tensors as $\boldsymbol{C} = \boldsymbol{F}^T \boldsymbol{F}$ and $\boldsymbol{B} = \boldsymbol{F} \boldsymbol{F}^T$.

For isotropic incompressible elasticity the constitutive equations can be written as a relationship between the Cauchy stress \boldsymbol{T} and \boldsymbol{B} as

$$\boldsymbol{T} = -\pi \boldsymbol{I} + \alpha_1 \boldsymbol{B} + \alpha_{-1} \boldsymbol{B}^{-1}, \quad \det \boldsymbol{B} = 1, \quad (2.1)$$

where π is an arbitrary Lagrangian multiplier representing a hydrostatic pressure and α_1 , α_{-1} are coefficients which may depend on the deformation.

Alternatively, the principal stresses T_i ($i = 1, 2, 3$), that are aligned with the Eulerian principal axes, can be obtained in terms of a strain-energy function W , which can be viewed as a function of the principal stretches λ_i

2. NOTATION AND GOVERNING EQUATIONS

($i = 1, 2, 3$). In the case of an incompressible material these relationships take the form (index i not summed)

$$T_i = -\pi + \lambda_i \frac{\partial W(\lambda_1, \lambda_2, \lambda_3)}{\partial \lambda_i}, \quad \lambda_1 \lambda_2 \lambda_3 = 1, \quad (2.2)$$

Eqs. (2.1) and (2.2) are linked through the following equations (Ref. [7])

$$\begin{aligned} \alpha_1 &= \frac{1}{\lambda_1^2 - \lambda_2^2} \left[\frac{(T_1 - T_3)\lambda_1^2}{\lambda_1^2 - \lambda_3^2} - \frac{(T_2 - T_3)\lambda_2^2}{\lambda_2^2 - \lambda_3^2} \right], \\ \alpha_{-1} &= \frac{1}{\lambda_1^2 - \lambda_2^2} \left[\frac{T_1 - T_3}{\lambda_1^2 - \lambda_3^2} - \frac{T_2 - T_3}{\lambda_2^2 - \lambda_3^2} \right], \end{aligned} \quad (2.3)$$

that allow to express coefficients α_1 , α_{-1} in terms of the strain energy of the body.

In the absence of body forces, equilibrium is expressed in terms of the first Piola-Kirchhoff stress tensor $\mathbf{S} = J \mathbf{T} \mathbf{F}^{-T}$ as $\text{Div} \mathbf{S} = \mathbf{0}$, where Div is the divergence operator defined in B_0 .

Loss of uniqueness of the plane-strain incremental boundary-value problem is investigated, so that incremental displacements are given by

$$\mathbf{u}(\mathbf{x}) = \dot{\boldsymbol{\xi}}(\mathbf{x}^0), \quad (2.4)$$

where, henceforth, a superposed dot is used to denote a first-order increment. The incremental counterpart of equilibrium is expressed by $\text{div} \boldsymbol{\Sigma} = \mathbf{0}$, where div is the divergence in the current configuration. The updated incremental first Piola-Kirchhoff stress is given by

$$\boldsymbol{\Sigma} = \dot{\mathbf{S}} \mathbf{F}^T, \quad \dot{\mathbf{S}} = \dot{\mathbf{T}} \mathbf{F}^{-T} - \mathbf{T} \mathbf{L}^T \mathbf{F}^{-T}. \quad (2.5)$$

The linearized constitutive equation is

$$\boldsymbol{\Sigma} = \mathbb{C} \mathbf{L} - \dot{\pi} \mathbf{I}, \quad (2.6)$$

where $\mathbf{L} = \text{grad} \mathbf{u}$ and \mathbb{C} is the fourth-order tensor of instantaneous elastic moduli (possessing the major symmetries). Incompressibility requires that

$\text{tr} \mathbf{L} = 0$. Since $\boldsymbol{\Sigma} = \dot{\mathbf{T}} - \mathbf{T} \mathbf{L}^T$, the balance of rotational momentum yields $\Sigma_{12} - \Sigma_{21} = T_2 L_{12} - T_1 L_{21}$, and a comparison with eq. (2.6) shows that (no sum on indices i and j)

$$C_{ijji} + T_i = C_{jiji} \quad (i \neq j). \quad (2.7)$$

For a hyperelastic material, the components of \mathbb{C} can be defined in terms of the strain-energy function W .

For the plane strain problem addressed here the fourth-order tensor \mathbb{C} can be written in terms of 2 incremental moduli μ and μ^* , their explicit form will be given

$$\mu = \frac{\lambda}{2} \left(\frac{\lambda^4 + 1}{\lambda^4 - 1} \frac{d\hat{W}}{d\lambda} \right), \quad \mu^* = \frac{\lambda}{4} \left(\frac{d\hat{W}}{d\lambda} + \lambda \frac{d^2 \hat{W}}{d\lambda^2} \right), \quad (2.8)$$

where $\hat{W} = W(\lambda, 1/\lambda, 1)$, due to incompressibility. In the following, examples are given for a neo-Hookean material, which is the initially isotropic elastic solid with strain energy given by

$$W = \frac{\mu_0}{2} (\lambda_1^2 + \lambda_2^2 - 2), \quad (2.9)$$

where λ_1 and λ_2 are the principal in-plane stretches. Due to incompressibility $\lambda = \lambda_1$ and $\lambda_2 = 1/\lambda$, so that

$$T_1 = \mu_0(\lambda^2 - \lambda^{-2}), \quad \text{and} \quad \mu = \mu^* = \frac{\mu_0}{2}(\lambda^2 + \lambda^{-2}), \quad (2.10)$$

where the former is the uniaxial tension law (along axis x_2). Notice that the ratio between T_1 and μ is

$$\frac{T_1}{\mu} = \frac{2(\lambda^2 - \lambda^{-2})}{\lambda^2 + \lambda^{-2}}, \quad (2.11)$$

and its value is always ranging between -2 (infinite compression, $\lambda \rightarrow 0$) and 2 (infinite tension, $\lambda \rightarrow +\infty$).

2. NOTATION AND GOVERNING EQUATIONS

In the case of an out-of-plane analysis the fourth-order tensor \mathbb{C} is dependent on six moduli μ_i and μ_i^* ($i = 1, 2, 3$) (no sum on index), see Refs. [11, 39], which for a hyperelastic material can be written as

$$\begin{aligned} 2\mu_i^* &= \lambda_i \frac{\partial W}{\partial \lambda_i} + \lambda_i^2 \frac{\partial^2 W}{\partial \lambda_i^2} - \sum_{l \neq i} \lambda_i \lambda_l \frac{\partial^2 W}{\partial \lambda_i \partial \lambda_l} + \lambda_j \lambda_k \frac{\partial^2 W}{\partial \lambda_j \partial \lambda_k} \quad (j \neq k \neq i), \\ 2\mu_i &= (T_j - T_k) \frac{\lambda_j^2 + \lambda_k^2}{\lambda_j^2 - \lambda_k^2} \quad (j \neq k \neq i). \end{aligned} \quad (2.12)$$

In the ensuing analysis of multilayers two types of interface conditions will be employed: perfect bonding, where both incremental tractions and displacements are continuous and imperfect interface (compliant interface), where the incremental shear stress is linearly dependent on the jump of incremental transverse displacement.

In the former case, where the layers are perfectly bonded, the imposed interfacial conditions are:

- continuity of tractions across the interface

$$\boldsymbol{\Sigma}^+ \mathbf{n} = \boldsymbol{\Sigma}^- \mathbf{n}; \quad (2.13)$$

- continuity of incremental displacements

$$\mathbf{u}^+ = \mathbf{u}^-. \quad (2.14)$$

In the latter case, we employ a particular case of the compliant interface model of Suo et al. and Bigoni et al. (Ref. [51] and [9]) for which, in addition to eqn. (2.13), the radial incremental displacement u_r is continuous across the interface while a compliant law relating the incremental shear stress to the transverse displacement jump is imposed, namely

$$\Sigma_{\theta r}^{(s)} \Big|_{r=r_e^{(s)}} = \mathcal{S}_\theta \left(u_\theta^{(s+1)+} - u_\theta^{(s)-} \right). \quad (2.15)$$

Here, \mathcal{S}_θ is the instantaneous interface stiffness of dimension [stress/length].

3

Finite pure bending of an elastic layered block

The solution for pure bending of an elastic layered thick plate made up of N layers follows from ‘assembling’ solutions relative to the bending of all layers taken separately, a solution first given by Rivlin (Ref. [42]). Therefore, we begin recalling this solution with reference now to a generic layer. To this purpose, we consider plane-strain flexure of an incompressible rectangular elastic layered plate, of initial dimensions $l_0 \times h_0$ (see Fig. 3.1b).

3.1 Kinematics

In the reference stress-free configuration, a Cartesian coordinate system $O_0^{(s)}x_1^{0(s)}x_2^{0(s)}x_3^{0(s)}$ is introduced for each layer denoted by index s , centered at its centroid (see Fig. 3.1a). Denoting by \mathbf{e}_i^0 ($i = 1, 2, 3$) the common cartesian basis, the position of the generic point $\mathbf{x}^{0(s)}$ is given by

$$\mathbf{x}^{0(s)} = x_1^{0(s)} \mathbf{e}_1^0 + x_2^{0(s)} \mathbf{e}_2^0 + x_3^{0(s)} \mathbf{e}_3^0, \quad (3.1)$$

with

$$x_1^{0(s)} \in [-h_0^{(s)}/2, h_0^{(s)}/2], \quad x_2^{0(s)} \in [-l_0/2, l_0/2], \quad x_3^{0(s)} \in (-\infty, +\infty). \quad (3.2)$$

3. FINITE BENDING OF A LAYERED BLOCK

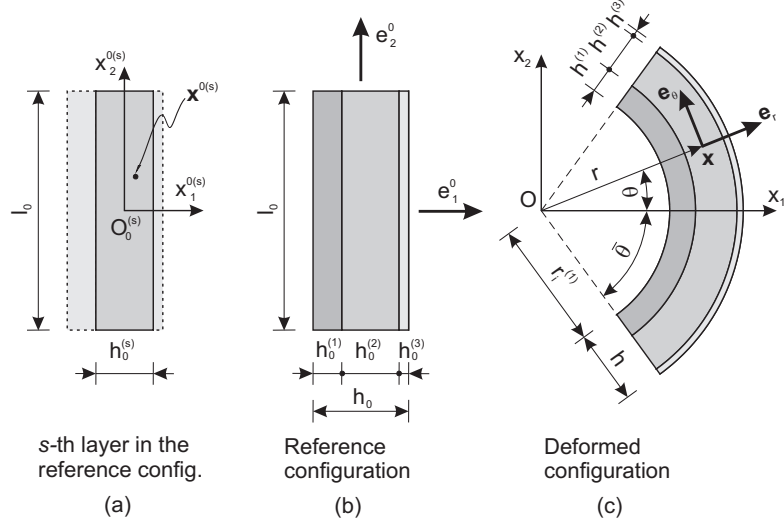


Figure 3.1: Sketch of a generic layered thick plate subject to finite bending.

The deformed configuration is a portion of a cylindrical tube of semi-angle $\bar{\theta}$. It is useful to introduce here a cylindrical coordinate system $O^{(s)}r^{(s)}\theta^{(s)}z^{(s)}$, with basis e_r , e_θ and e_z , where points of the s -th layer are transformed to points identified by

$$r^{(s)} \in [r_i^{(s)}, r_i^{(s)} + h^{(s)}], \quad \theta^{(s)} \in [-\bar{\theta}, +\bar{\theta}], \quad z^{(s)} \in (-\infty, +\infty).$$

The deformation is prescribed in a way that a plane at constant $x_1^{0(s)}$ transforms to a circular arc at constant $r^{(s)}$, while a plane at constant $x_2^{0(s)}$ transforms to a plane at constant $\theta^{(s)}$. The out-of-plane deformation is null, so that $x_3^{0(s)} = z^{(s)}$. The incompressibility constraint (conservation of areas) imposes that

$$r_i^{(s)} = \frac{l_0 h_0^{(s)}}{2\bar{\theta} h^{(s)}} - \frac{h^{(s)}}{2}, \quad (3.3)$$

where $h^{(s)}$ is the current thickness of the circular sector, to be determined. The deformation, in this condition, is described by functions

$$r^{(s)} = r^{(s)}(x_1^{0(s)}), \quad \theta^{(s)} = \theta^{(s)}(x_2^{0(s)}), \quad z^{(s)} = x_3^{0(s)}, \quad (3.4)$$

so that the deformation gradient takes the form

$$\mathbf{F}^{(s)} = \frac{dr^{(s)}}{dx_1^{0(s)}} \mathbf{e}_r \otimes \mathbf{e}_1^0 + r^{(s)} \frac{d\theta^{(s)}}{dx_2^{0(s)}} \mathbf{e}_\theta \otimes \mathbf{e}_2^0 + \mathbf{e}_z \otimes \mathbf{e}_3^0. \quad (3.5)$$

The right and left Cauchy-Green tensors are

$$\begin{aligned} \mathbf{C}^{(s)} &= \left(\frac{dr^{(s)}}{dx_1^{0(s)}} \right)^2 \mathbf{e}_1^0 \otimes \mathbf{e}_1^0 + \left(r^{(s)} \frac{d\theta^{(s)}}{dx_2^{0(s)}} \right)^2 \mathbf{e}_2^0 \otimes \mathbf{e}_2^0 + \mathbf{e}_3^0 \otimes \mathbf{e}_3^0, \\ \mathbf{B}^{(s)} &= \left(\frac{dr^{(s)}}{dx_1^{0(s)}} \right)^2 \mathbf{e}_r \otimes \mathbf{e}_r + \left(r^{(s)} \frac{d\theta^{(s)}}{dx_2^{0(s)}} \right)^2 \mathbf{e}_\theta \otimes \mathbf{e}_\theta + \mathbf{e}_z \otimes \mathbf{e}_z, \end{aligned} \quad (3.6)$$

so that we identify the principal stretches to be

$$\lambda_r^{(s)} = \frac{dr^{(s)}}{dx_1^{0(s)}}, \quad \lambda_\theta^{(s)} = r^{(s)} \frac{d\theta^{(s)}}{dx_2^{0(s)}}, \quad \text{and} \quad \lambda_z^{(s)} = 1. \quad (3.7)$$

Imposition of the incompressibility constraint reduces the deformation to the simple form

$$r^{(s)} = \sqrt{\frac{2}{\alpha^{(s)}} x_1^{0(s)} + \beta^{(s)}}, \quad \theta^{(s)} = \alpha^{(s)} x_2^{0(s)}, \quad (3.8)$$

so that, using eqn. (3.4), the principal stretches can be evaluated as

$$\lambda_r^{(s)} = \frac{1}{\alpha^{(s)} r^{(s)}}, \quad \lambda_\theta^{(s)} = \alpha^{(s)} r^{(s)}, \quad \text{and} \quad \lambda_z^{(s)} = 1, \quad (3.9)$$

where $\alpha^{(s)}$ and $\beta^{(s)}$ are constants which are fixed by boundary conditions.

For the s -th layer of a multilaminated, these are

- at $x_2^{0(s)} = \pm l_0/2$, $\theta^{(s)} = \pm \bar{\theta}$, from eqn. (3.8)₂, $\theta^{(s)} = \pm \alpha^{(s)} l_0/2$, yielding

$$\alpha^{(s)} = \frac{2\bar{\theta}}{l_0}; \quad (3.10)$$

note that $\alpha^{(s)}$ is independent of the index s ;

- at $x_1^{0(s)} = -h_0^{(s)}/2$, $r^{(s)} = r_i^{(s)}$, from eqns. (3.3) and (3.8)₁, $r_i^{(s)} = r^{(s)}(-h_0^{(s)}/2)$, yielding

$$\beta^{(s)} = r_i^{(s)2} + \frac{l_0 h_0^{(s)}}{2\theta}. \quad (3.11)$$

3. FINITE BENDING OF A LAYERED BLOCK

Since the N layers are assumed to be perfectly bonded to each other and the s -th layer has current thickness $h^{(s)}$, we have

$$r_i^{(s)} = r_i^{(s-1)} + h^{(s-1)} \quad (s = 2, \dots, N), \quad (3.12)$$

with $r_i^{(1)}$ given by $r_i^{(1)} = l_0 h_0^{(1)} / (2\bar{\theta} h^{(1)}) - h^{(1)} / 2$, see eqn. (3.3). A repeated use of eqns. (3.3) and (3.12) provides all thicknesses $h^{(s)}$ ($s = 2, \dots, N$) expressed in terms of the thickness of the first layer $h^{(1)}$, which remains the sole kinematical unknown of the problem, determined from the solution of the boundary-value problem described in Section 3.2.

Since eqn. (3.12) is imposed at each of the $N - 1$ interfaces between layers, all radial coordinates $r^{(s)}$ share the same origin O of a new cylindrical coordinate system $Or\theta z$, common to all deformed layers (Fig. 3.1c); therefore, index s on the local current coordinates will be omitted in the following so that the deformed configuration will be described in terms of the global system $Or\theta z$.

As a conclusion, the kinematics provides all the stretches in the multi-layered which can be represented as

$$\lambda_r = \frac{l_0}{2\bar{\theta}r}, \quad \lambda_\theta = \frac{2\bar{\theta}r}{l_0}, \quad \text{and} \quad \lambda_z = 1, \quad (3.13)$$

and the current thickness of the s -th layer, $h^{(s)}$, as a function of $h^{(s-1)}$, namely

$$h^{(s)} = -\frac{l_0 h_0^{(s-1)}}{2\bar{\theta} h^{(s-1)}} - \frac{h^{(s-1)}}{2} + \sqrt{\left(\frac{l_0 h_0^{(s-1)}}{2\bar{\theta} h^{(s-1)}} + \frac{h^{(s-1)}}{2}\right)^2 - \frac{l_0 h_0^{(s)}}{\bar{\theta}}} \quad (s = 2, \dots, N). \quad (3.14)$$

Therefore all current thicknesses are known once the thickness of the first layer, $h^{(1)}$, is known.

3.2 Stress

We are now in a position to determine the stress state within the multilayer. In particular, the Cauchy stress tensor in generic layer s can be written as

$$\mathbf{T}^{(s)} = T_r^{(s)} \mathbf{e}_r \otimes \mathbf{e}_r + T_\theta^{(s)} \mathbf{e}_\theta \otimes \mathbf{e}_\theta + T_z^{(s)} \mathbf{e}_z \otimes \mathbf{e}_z, \quad (3.15)$$

where, from the constitutive equations (2.2),

$$T_r^{(s)} = -\pi^{(s)} + \lambda_r \frac{\partial W^{(s)}}{\partial \lambda_r}, \quad T_\theta^{(s)} = -\pi^{(s)} + \lambda_\theta \frac{\partial W^{(s)}}{\partial \lambda_\theta}, \quad (3.16)$$

$$T_z^{(s)} = -\pi^{(s)} + \frac{\partial W^{(s)}}{\partial \lambda_z} \Big|_{\lambda_z=1}.$$

Since stretches depend only on r , the chain rule of differentiation

$$\frac{d \cdot}{dr} = \frac{\partial \cdot}{\partial \lambda_r} \frac{d \lambda_r}{dr} + \frac{\partial \cdot}{\partial \lambda_\theta} \frac{d \lambda_\theta}{dr}, \quad (3.17)$$

together with eqns. (3.16) and the derivatives of stretches with respect to r calculated from eqn. (3.9), can be used in the equilibrium equations

$$\frac{\partial T_r^{(s)}}{\partial r} + \frac{T_r^{(s)} - T_\theta^{(s)}}{r} = 0, \quad \frac{\partial T_\theta^{(s)}}{\partial \theta} = 0, \quad (3.18)$$

to obtain the identities

$$\frac{dW^{(s)}}{dr} = -\frac{T_r^{(s)} - T_\theta^{(s)}}{r} = \frac{dT_r^{(s)}}{dr}. \quad (3.19)$$

Therefore, identifying λ_θ with λ , we arrive at the expression

$$T_r^{(s)}(r) = \hat{W}^{(s)}(\lambda(r)) + \gamma^{(s)}, \quad (3.20)$$

where

$$\hat{W}^{(s)}(\lambda(r)) = W^{(s)}(1/\lambda(r), \lambda(r), 1), \quad (3.21)$$

and $\gamma^{(s)}$ is an unknown integration constant. From eqn. (3.18)₁ we finally obtain

$$T_\theta^{(s)}(r) = \frac{2\bar{\theta}}{l_0} r \left(\hat{W}^{(s)} \right)' + \hat{W}^{(s)} + \gamma^{(s)}, \quad (3.22)$$

3. FINITE BENDING OF A LAYERED BLOCK

where the prime denotes, now, differentiation with respect to λ

Constants $\gamma^{(s)}$ ($s = 1, \dots, N$) and thickness $h^{(1)}$ can be calculated by imposing: (i.) continuity of tractions at interfaces between layers ($N - 1$ equations) and (ii.) traction boundary conditions at the external boundaries of the multilayer (2 equations). Considering N layers, the traction continuity at the interfaces write as

$$T_r^{(s-1)}(r_i^{(s-1)} + h^{(s-1)}) = T_r^{(s)}(r_i^{(s)}) \quad (s = 2, \dots, N), \quad (3.23)$$

while null loading at the external surfaces of the multilayer yields

$$T_r^{(1)}(r_i^{(1)}) = 0, \quad T_r^{(N)}(r_i^{(N)} + h^{(N)}) = 0. \quad (3.24)$$

Therefore, $\gamma^{(N)}$ can be calculated from eqn. (3.24)₂

$$\gamma^{(N)} = -\hat{W}^{(N)} \left(\lambda(r_i^{(N)} + h^{(N)}) \right), \quad (3.25)$$

while employing eqn. (3.23), we obtain the recursive formulae

$$\gamma^{(s-1)} = \hat{W}^{(s)} \left(\lambda(r_i^{(s)}) \right) - \hat{W}^{(s-1)} \left(\lambda(r_i^{(s)}) \right) + \gamma^{(s)} \quad (s = 2, \dots, N). \quad (3.26)$$

Considering now eqn. (3.24)₁ and evaluating $\gamma^{(1)}$ from eqn. (3.26) written for $s = 2$, we obtain an implicit expression to be solved for $h^{(1)}$

$$\hat{W}^{(2)} \left(\lambda(r_i^{(2)}) \right) - \hat{W}^{(1)} \left(\lambda(r_i^{(2)}) \right) + \hat{W}^{(1)} \left(\lambda(r_i^{(1)}) \right) + \gamma^{(2)} = 0, \quad (3.27)$$

where $h^{(2)}$ and $\gamma^{(2)}$ are functions of $h^{(1)}$, through eqns. (3.14) and (3.26), respectively.

Note that if the strain-energy function is the same for all layers, the multilayer corresponds to a homogeneous elastic block with thickness equal to the sum of all $h^{(s)}$; in this case eqn. (3.26) shows that $\gamma^{(s)} = \gamma^{(N)}$, for every s , and the uniform layer solution is recovered.

3.3 Examples of multilayered plates under finite bending

The solution obtained in the previous section is interesting in itself and can be easily used for design purposes, since it allows determination of the complex stress and strain fields within a thick, multilayered plate, when subject to finite bending. To highlight the usefulness of the solution, we present a few results for finite bending of an elastic thick plate, coated with a thin and stiff layer, and of a three- and five- layer structures, assuming a neo-Hookean behaviour for both materials.

Deformed geometries for the coated layer (with $l_0/h_0 = 2$, $h_0^{(lay)}/h_0^{(coat)} = 10$ and $\mu^{(coat)}/\mu^{(lay)} = 20$) are shown in Fig. 3.2, together with graphs of the dimensionless Cauchy principal stresses $T_r(r)/\mu^{(lay)}$ and $T_\theta(r)/\mu^{(lay)}$. The deformed configurations plotted in the upper part of Fig. 3.2 correspond to critical configurations at bifurcation (see Section 4.2), while those reported in the lower part lie beyond the critical bifurcation threshold, so that they are reported only with the purpose to show the evolution of the solution of finite bending at very large angles. Note that the transverse stress is always compressive, while the distribution of $T_\theta(r)$ strongly depends on the stiffness of the layer under consideration and gives a null resultant, so that it is equivalent to the bending moment loading the plate. For all cases, the neutral axis (the line corresponding to vanishing circumferential stress) is drawn, showing the effect of the coating on the global stress state. Note that in the lower figure on the left, *two neutral axes* are visible. This is an important feature, which is also investigated in Fig. 3.3, referred to a three-layer plate. In this structure, where the initial aspect ratio is 1, the shear stiffness contrast is 20 and ratio between layer thicknesses is 5, *three neutral axes* become visible starting from a bending semi-angle of 56° , so that to give evidence to this effect a bending semi-angle of 90° is imposed in Fig. 3.3. Finally, a complex situation with 5 layers with initial aspect ratio

3. FINITE BENDING OF A LAYERED BLOCK

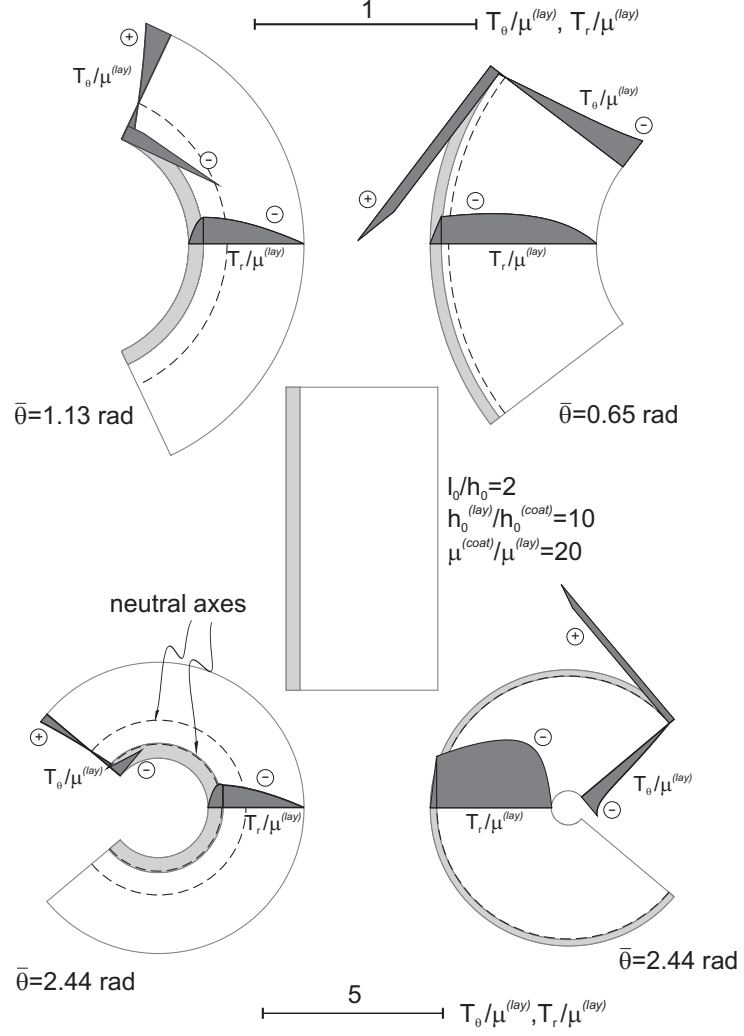


Figure 3.2: Undeformed (center) and deformed (upper and lower parts) shapes and internal stress states for finite bending of neo-Hookean coated plates with $l_0/h_0 = 2$, $h_0^{(lay)}/h_0^{(coat)} = 10$ and $\mu^{(coat)}/\mu^{(lay)} = 20$. Dashed lines represent the neutral axes. Note that in the picture in the lower part on the right the neutral axis is almost coincident with the interface between the two layers, while on the left two neutral axes are visible. Note the scales of diagrams for dimensionless stresses.

3.3 Examples of multilayered plates under finite bending

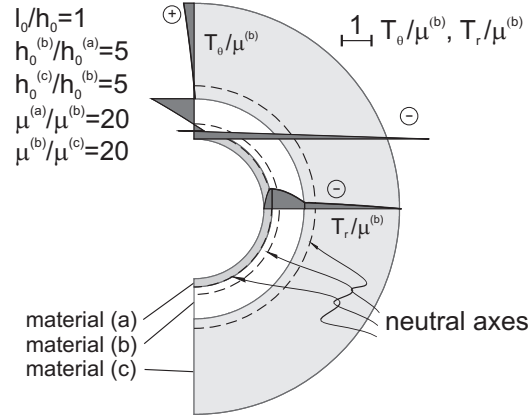


Figure 3.3: Finite bending of a neo-Hookean three-layer plate showing three neutral axes.

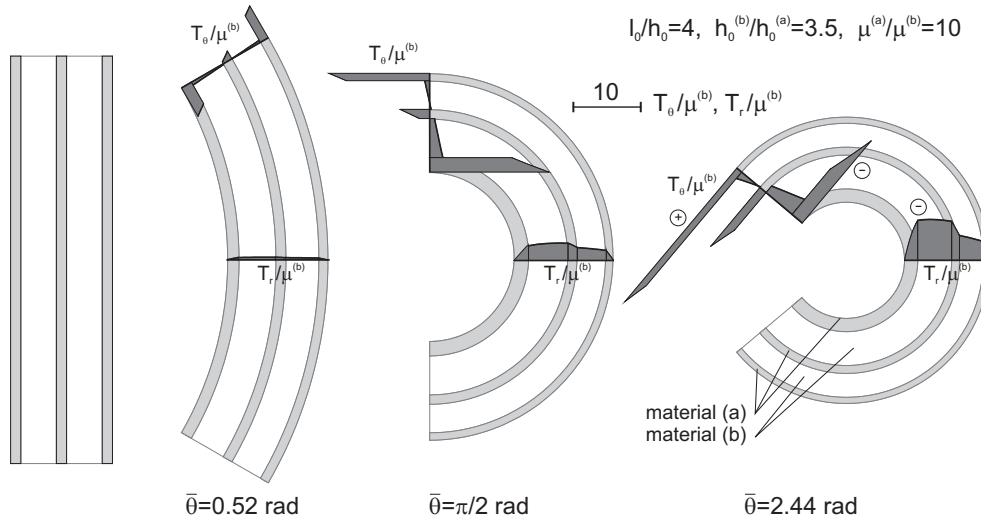


Figure 3.4: From left to right: undeformed and progressively more deformed shapes and internal stress states for finite bending of a neo-Hookean five-layer plate with $l_0/h_0 = 4$, $h_0^{(b)}/h_0^{(a)} = 3.5$, $\mu^{(a)}/\mu^{(b)} = 10$. Note the scales of diagrams for dimensionless stresses.

3. FINITE BENDING OF A LAYERED BLOCK

$l_0/h_0 = 4$ is reported in Fig. 3.4, where three configurations are shown at different bending angles $\bar{\theta}$. The layers are made up of two materials, (a) and (b), such that $h_0^{(b)}/h_0^{(a)} = 3.5$ and $\mu^{(a)}/\mu^{(b)} = 10$. As in Fig. 3.2, the two principal components of the Cauchy stress are drawn. A peculiar feature of the stress state is the positive sign of the circumferential stress $T_\theta(r)$ in the inner, stiff layer, to be compared to the negative sign in the two adjacent layers. This situation once more confirms the presence of two neutral axes, one of which in this case is ‘virtual’, in the sense that it is obtained joining the ‘peaks’ of the diagram of the positive stresses.

4

In-plane incremental bifurcations superimposed on finite bending of an elastic layered block

The goal of this section is to address the plane-strain bifurcation problem of the multilayered thick plate subject to finite bending, considered in Chapter 3.

4.1 General formulation

We begin by analyzing the incremental field equations for an isolated layer and we continue formulating the multilayered problem by adding the relevant interfacial and external boundary conditions. We refer to Chapter 2 for the notation.

The gradient of incremental displacement $\mathbf{u}(\mathbf{x})$ is

$$\mathbf{L} = u_{r,r} \mathbf{e}_r \otimes \mathbf{e}_r + \frac{u_{r,\theta} - u_\theta}{r} \mathbf{e}_r \otimes \mathbf{e}_\theta + u_{\theta,r} \mathbf{e}_\theta \otimes \mathbf{e}_r + \frac{u_r + u_{\theta,\theta}}{r} \mathbf{e}_\theta \otimes \mathbf{e}_\theta, \quad (4.1)$$

4. IN-PLANE INCREMENTAL BIFURCATIONS

and the incompressibility condition ($\text{tr} \mathbf{L} = 0$) can be written in polar coordinates as

$$r u_{r,r} + u_r + u_{\theta,\theta} = 0. \quad (4.2)$$

For an incompressible isotropic elastic material, the components of the constitutive fourth-order tensor \mathbb{C} [see eqn. (2.6)] can be written as function of two incremental moduli, denoted μ and μ_* , that depend on the deformation. The non-vanishing components of \mathbb{C} may be expressed as

$$\begin{aligned} C_{rrrr} = C_{\theta\theta\theta\theta} &= 2\mu_* + p, & C_{\theta r \theta r} &= \mu - \Gamma, \\ C_{r \theta r \theta} &= \mu + \Gamma, & C_{r \theta \theta r} = C_{\theta r r \theta} &= \mu + p, \end{aligned} \quad (4.3)$$

where

$$\Gamma = \frac{T_\theta - T_r}{2}, \quad p = -\frac{T_\theta + T_r}{2} \quad (4.4)$$

describe the state of prestress. For hyperelastic materials, μ and μ_* can be given in terms of the strain-energy function $\hat{W}(\lambda)$ as

$$\mu = \frac{\lambda}{2} \left(\frac{\lambda^4 + 1}{\lambda^4 - 1} \frac{d\hat{W}}{d\lambda} \right), \quad \mu_* = \frac{\lambda}{4} \left(\frac{d\hat{W}}{d\lambda} + \lambda \frac{d^2\hat{W}}{d\lambda^2} \right). \quad (4.5)$$

The incremental constitutive equations in terms of the incremental first Piola-Kirchhoff stress tensor can be written as

$$\begin{aligned} \Sigma_{rr} &= -\dot{\pi} + (2\mu_* + p)u_{r,r}, & \Sigma_{\theta\theta} &= -\dot{\pi} + (2\mu_* + p)\frac{u_r + u_{\theta,\theta}}{r}, \\ \Sigma_{r\theta} &= (\mu + \Gamma)\frac{u_{r,\theta} - u_\theta}{r} + (\mu + p)u_{\theta,r}, & \Sigma_{\theta r} &= (\mu + p)\frac{u_{r,\theta} - u_\theta}{r} + (\mu - \Gamma)u_{\theta,r}. \end{aligned} \quad (4.6)$$

A substitution of eqns. (4.6) and the use of eqn. (3.18)₁ in the incremental equations of equilibrium written in polar coordinates

$$\begin{aligned} \Sigma_{rr,r} + \frac{1}{r}\Sigma_{r\theta,\theta} + \frac{\Sigma_{rr} - \Sigma_{\theta\theta}}{r} &= 0, \\ \Sigma_{\theta r,r} + \frac{1}{r}\Sigma_{\theta\theta,\theta} + \frac{\Sigma_{\theta r} + \Sigma_{r\theta}}{r} &= 0, \end{aligned} \quad (4.7)$$

4.1 General formulation

yields the incremental equilibrium equations written in terms of incremental displacements and in-plane mean stress

$$\begin{aligned}\dot{\pi}_{,r} &= \left\{ (p + 2\mu_*)_{,r} + \frac{2(p + 2\mu_*)}{r} \right\} u_{r,r} + (p + 2\mu_*)u_{r,rr} \\ &\quad + (\mu + \Gamma) \frac{u_{r,\theta\theta} - u_{\theta,\theta}}{r^2} + (p + \mu) \frac{u_{\theta,r\theta}}{r}, \\ \dot{\pi}_{,\theta} &= [r(\mu - \Gamma)_{,r} + \mu - \Gamma] \left(u_{\theta,r} + \frac{u_{r,\theta} - u_{\theta}}{r} \right) + r(\mu - \Gamma)u_{\theta,rr} + (\mu - 2\mu_*)u_{r,\theta r}.\end{aligned}\tag{4.8}$$

We seek bifurcations in the following separable-variables form

$$\begin{cases} u_r(r, \theta) = f(r) \cos n\theta, \\ u_\theta(r, \theta) = g(r) \sin n\theta, \\ \dot{\pi}(r, \theta) = k(r) \cos n\theta, \end{cases}\tag{4.9}$$

where $f(r)$, $g(r)$ and $k(r)$ are real functions and n is a real number to be determined by imposing boundary conditions.

Consideration of the incompressibility constraint

$$g = -\frac{(f + rf')}{n},\tag{4.10}$$

and substitution of representations (4.9) into eqns. (4.8) yields

$$\begin{aligned}k' &= Df'' + \left(C_{,r} + D_{,r} + \frac{C + 2D}{r} \right) f' + \frac{E(1 - n^2)}{r^2} f, \\ k &= \frac{r^2 C}{n^2} f''' + \frac{F + 3C}{n^2} r f'' + \left(\frac{F}{n^2} - D \right) f' - \frac{1 - n^2}{n^2} \frac{F}{r} f,\end{aligned}\tag{4.11}$$

where a prime denotes differentiation with respect to r and in terms of incremental moduli μ and μ_* and strain-energy function $\hat{W}(\lambda)$, the coefficients C , D , E and F can be expressed as

$$\begin{aligned}C = \mu - \Gamma &= \frac{\lambda}{\lambda^4 - 1} \frac{d\hat{W}}{d\lambda}, & D = 2\mu_* - \mu &= \frac{\lambda}{2} \left(\lambda \frac{d^2\hat{W}}{d\lambda^2} - \frac{2}{\lambda^4 - 1} \frac{d\hat{W}}{d\lambda} \right), \\ E = \mu + \Gamma &= \frac{\lambda^5}{\lambda^4 - 1} \frac{d\hat{W}}{d\lambda}, & F &= rC_{,r} + C.\end{aligned}\tag{4.12}$$

4. IN-PLANE INCREMENTAL BIFURCATIONS

By differentiating eqn. (4.11)₂ with respect to r and substituting it into eqn. (4.11)₁, a single differential equation in terms of $f(r)$ is obtained

$$\begin{aligned} Cr^4 f'''' + 2(F + 2C)r^3 f''' + [(rF)_{,r} + 4F - 2n^2 D]r^2 f'' \\ + [(rF - 2rn^2 D)_{,r} - 2F]r f' + (1 - n^2)(F - rF_{,r} - n^2 E)f = 0. \end{aligned} \quad (4.13)$$

Eqn. (4.13) defines the function $f(r)$ within a generic layer. Once $f(r)$ is known, the other functions, $g(r)$ and $k(r)$, can be calculated by employing eqns. (4.10) and (4.11)₂, respectively. The set of all functions $f^{(s)}(r)$ ($s = 1, \dots, N$) can be obtained imposing the continuity conditions at the interfaces and the boundary conditions at the external surfaces.

In the case of perfect bonding the continuity of incremental tractions and displacements at interfaces is imposed, which correspond to

$$\begin{aligned} u_r^{(s)} \Big|_{r=r_e^{(s)}} = u_r^{(s+1)} \Big|_{r=r_i^{(s+1)}}, \quad u_\theta^{(s)} \Big|_{r=r_e^{(s)}} = u_\theta^{(s+1)} \Big|_{r=r_i^{(s+1)}}, \\ \Sigma_{rr}^{(s)} \Big|_{r=r_e^{(s)}} = \Sigma_{rr}^{(s+1)} \Big|_{r=r_i^{(s+1)}}, \quad \Sigma_{\theta r}^{(s)} \Big|_{r=r_e^{(s)}} = \Sigma_{\theta r}^{(s+1)} \Big|_{r=r_i^{(s+1)}}, \end{aligned} \quad (4.14)$$

where $r_e^{(s)} = r_i^{(s)} + h^{(s)}$ or, in terms of functions defined in eqn. (4.9),

$$\begin{aligned} f^{(s)} \Big|_{r=r_e^{(s)}} = f^{(s+1)} \Big|_{r=r_i^{(s+1)}}, \quad g^{(s)} \Big|_{r=r_e^{(s)}} = g^{(s+1)} \Big|_{r=r_i^{(s+1)}}, \\ \{(p + 2\mu_*)f' - k\}^{(s)} \Big|_{r=r_e^{(s)}} = \{(p + 2\mu_*)f' - k\}^{(s+1)} \Big|_{r=r_i^{(s+1)}}, \\ \left\{ Cg' - \frac{1}{r}(nf + g)(p + \mu) \right\}^{(s)} \Big|_{r=r_e^{(s)}} = \left\{ Cg' - \frac{1}{r}(nf + g)(p + \mu) \right\}^{(s+1)} \Big|_{r=r_i^{(s+1)}}. \end{aligned} \quad (4.15)$$

The case of imperfect interface is ensured employing the following boundary conditions:

- continuity of incremental tractions at interfaces:

$$\Sigma_{rr}^{(s)} \Big|_{r=r_e^{(s)}} = \Sigma_{rr}^{(s+1)} \Big|_{r=r_i^{(s+1)}}, \quad \Sigma_{\theta r}^{(s)} \Big|_{r=r_e^{(s)}} = \Sigma_{\theta r}^{(s+1)} \Big|_{r=r_i^{(s+1)}}; \quad (4.16)$$

4.1 General formulation

- continuity of the radial component of the incremental displacement at interfaces;

$$u_r^{(s)} \Big|_{r=r_e^{(s)}} = u_r^{(s+1)} \Big|_{r=r_i^{(s+1)}}, \quad (4.17)$$

- imperfect ‘shear-type’ interface, see eqn. (2.15),

$$\Sigma_{\theta r}^{(s)} \Big|_{r=r_e^{(s)}} = \mathcal{S}_\theta \left(u_\theta^{(s+1)+} - u_\theta^{(s)-} \right), \quad (4.18)$$

where \mathcal{S}_θ is a shear stiffness, so that perfect bonding is recovered in the limit $\mathcal{S}_\theta \rightarrow \infty$;

For dead-load tractions on the external surfaces, the boundary conditions at $r = r_i^{(1)}$ and $r = r_e^{(N)}$ are

$$\Sigma_{rr}^{(1),(N)} \Big|_{r=r_i^{(1)}, r_e^{(N)}} = 0, \quad \Sigma_{\theta r}^{(1),(N)} \Big|_{r=r_i^{(1)}, r_e^{(N)}} = 0, \quad (4.19)$$

or, equivalently,

$$\begin{aligned} \{ (p + 2\mu_*)f' - k \}^{(1),(N)} \Big|_{r=r_i^{(1)}, r_e^{(N)}} &= 0, \\ \left\{ Cg' - \frac{1}{r}(nf + g)(p + \mu) \right\}^{(1),(N)} \Big|_{r=r_i^{(1)}, r_e^{(N)}} &= 0. \end{aligned} \quad (4.20)$$

On the boundaries $\theta = \pm\bar{\theta}$ we require that shear stresses and incremental normal displacements vanish, namely

$$\Sigma_{r\theta}^{(s)} \Big|_{\theta=\pm\bar{\theta}} = 0, \quad u_\theta^{(s)} \Big|_{\theta=\pm\bar{\theta}} = 0, \quad (4.21)$$

a condition which is achieved if $\sin n\bar{\theta} = 0$ [see eqn. (4.9)] or, equivalently, using eqn. (3.10), if

$$n = \frac{2m\pi}{\alpha l_0} \quad (m \in \mathbb{N}). \quad (4.22)$$

Since our objective is to employ a numerical method to evaluate the critical angle for bifurcation $\bar{\theta}_{cr}$, it becomes instrumental to rewrite eqn. (4.13) as a linear system of first-order ODEs. This and the procedure to derive numerically the bifurcation condition is described in Chapter 5.

4. IN-PLANE INCREMENTAL BIFURCATIONS

Eqn. (5.14) provides the critical angle for bifurcation, $\bar{\theta}_{cr}$, for a multi-layered elastic plate subject to bending in terms of initial aspect ratios and stiffness contrast between layers. Once this angle is known, eqn. (3.13)₂ yields the critical stretch $\lambda_{cr} = 2\bar{\theta}_{cr}r_i^{(1)}/l_0$.

4.2 Bifurcation of a bilayer

Although our analysis covers the case of a N -layer system, we will limit examples to the simple geometry of a two-layered system, also experimentally investigated, where one of the layers is taken thin and rigid with respect to the other, so that it acts as a sort of stiff coating. Both layers are made up of neo-Hookean material (for which the response always remains elliptic).

The critical angle $\bar{\theta}_{cr}$ and the critical stretch λ_{cr} (at the compressive side of the specimen) at bifurcation are reported in Figs. 4.1 and 4.2 as functions of the aspect ratio l_0/h_0 (unloaded height of the specimen is l_0 and global thickness is h_0 , see Fig. 3.1), for the thickness and stiffness ratios $h_0^{(lay)}/h_0^{(coat)} = 10$ and $\mu^{(coat)}/\mu^{(lay)} = 20$, respectively. In the figures, bifurcation curves are reported for different values of the integer parameter m which, through eqn. (4.22), defines the circumferential wavenumber n . Obviously, for a given value of l_0/h_0 the bifurcation threshold is set by the value of m providing the minimum (or maximum) value of the critical angle (or stretch). The difference between Fig. 4.1 and Fig. 4.2 is that the coating layer is at the tensile side of the specimen in the former case, while it is at the compressive side in the latter. In the same figures, also the threshold is reported for surface instability of the ‘soft’ layer material ($\lambda_{surf} \approx 0.545$, Ref. [11]). It can be deduced from the figures that a diffuse mode setting the bifurcation threshold always exists before surface instability, for each aspect ratio l_0/h_0 ¹. It is important to observe that the occurrence of the

¹ For a single elastic block, Triantafyllidis, Ref. [52], claims that surface instability occurs before diffuse modes, while Coman and Destrade, Ref. [17], on the contrary demonstrate that the first instability mode is diffused. However, the two points of view can be

4.2 Bifurcation of a bilayer

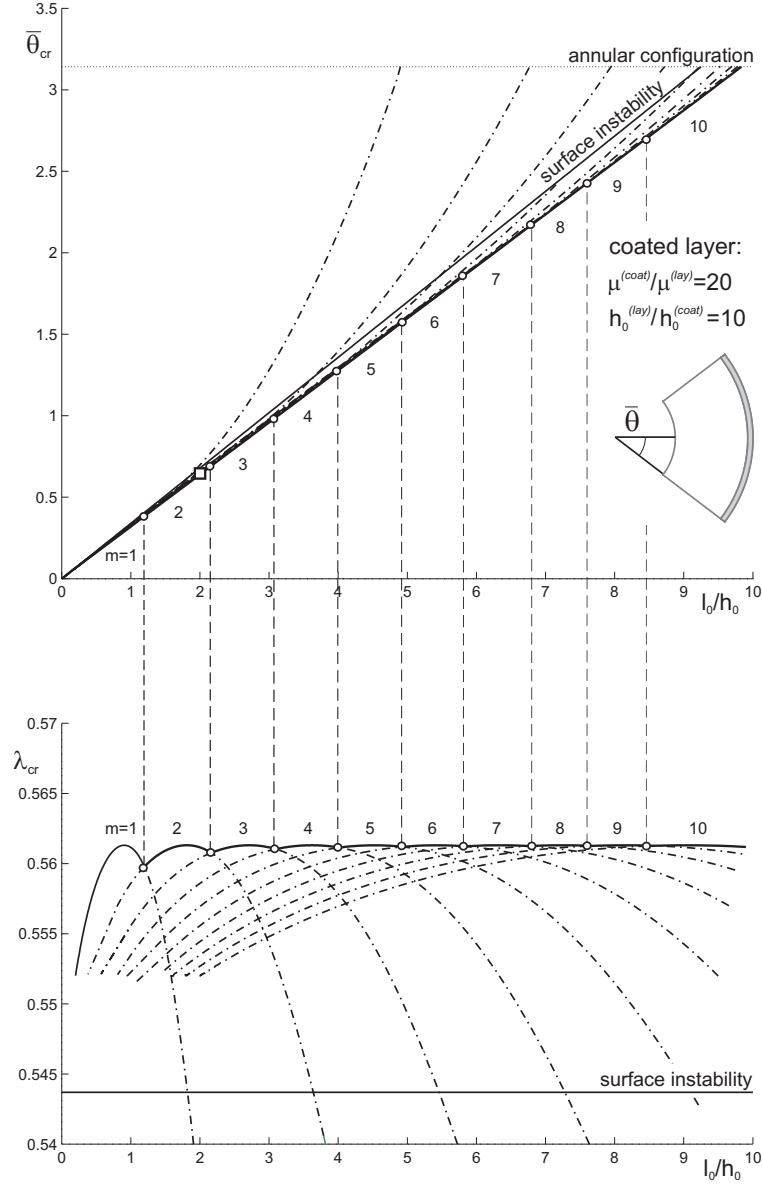


Figure 4.1: Critical angle $\bar{\theta}_{cr}$ and critical stretch λ_{cr} (evaluated at the internal boundary, $r = r_i^{(1)}$) versus aspect ratio l_0/h_0 of a neo-Hookean coated bilayer subject to bending with $h_0^{(lay)}/h_0^{(coat)} = 10$ and $\mu^{(coat)}/\mu^{(lay)} = 20$. The coating is located at the tensile side. In both plots, a small circle denotes a transition between two different integer values of m (the parameter which sets the circumferential wavenumber). The small ‘square’ on the bifurcation curve indicates the configuration studied in Fig. 3.2, top-left position.

4. IN-PLANE INCREMENTAL BIFURCATIONS

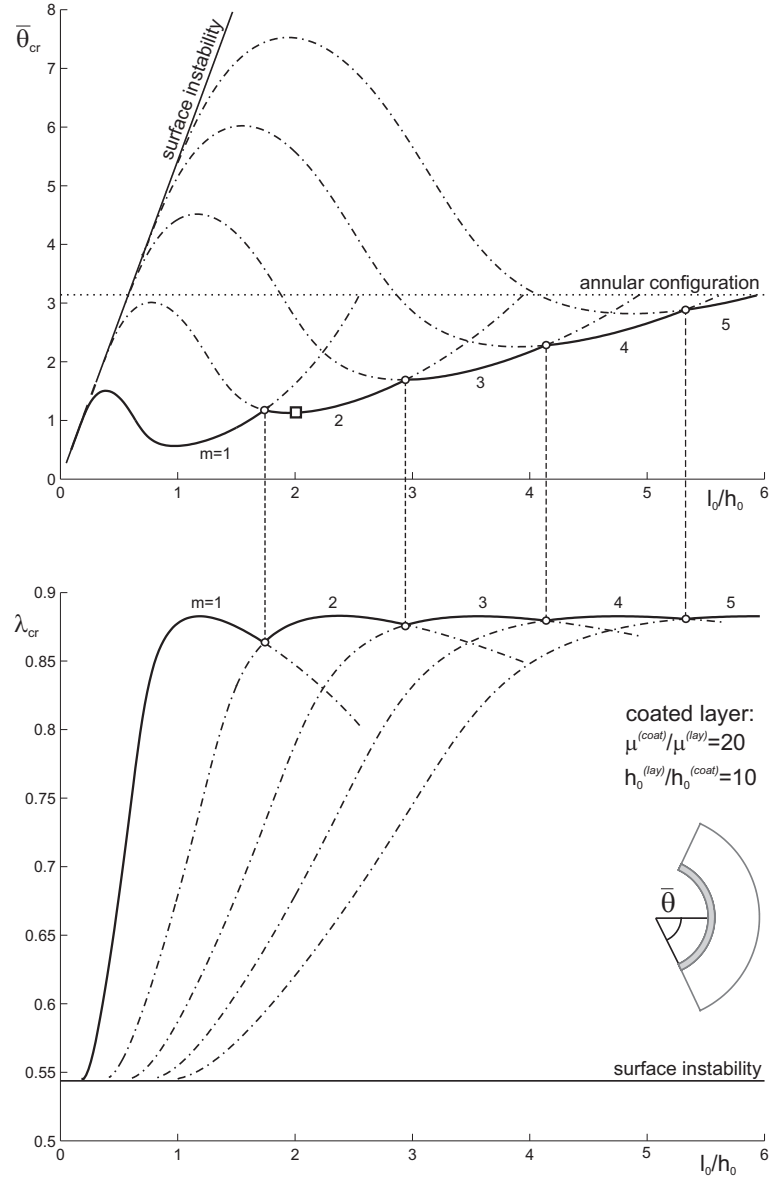


Figure 4.2: Critical angle $\bar{\theta}_{cr}$ and critical stretch λ_{cr} (evaluated at the internal boundary, $r = r_i^{(1)}$) versus aspect ratio l_0/h_0 of a neo-Hookean coated bilayer subject to bending with $h_0^{(lay)}/h_0^{(coat)} = 10$ and $\mu^{(coat)}/\mu^{(lay)} = 20$. The coating is located at the compressed side. In both plots, a small circle denotes a transition between two integer values of m (the parameter which sets the circumferential wavenumber). The small ‘square’ on the bifurcation curve indicates the configuration studied in Fig. 3.2, top-right position.

4.2 Bifurcation of a bilayer

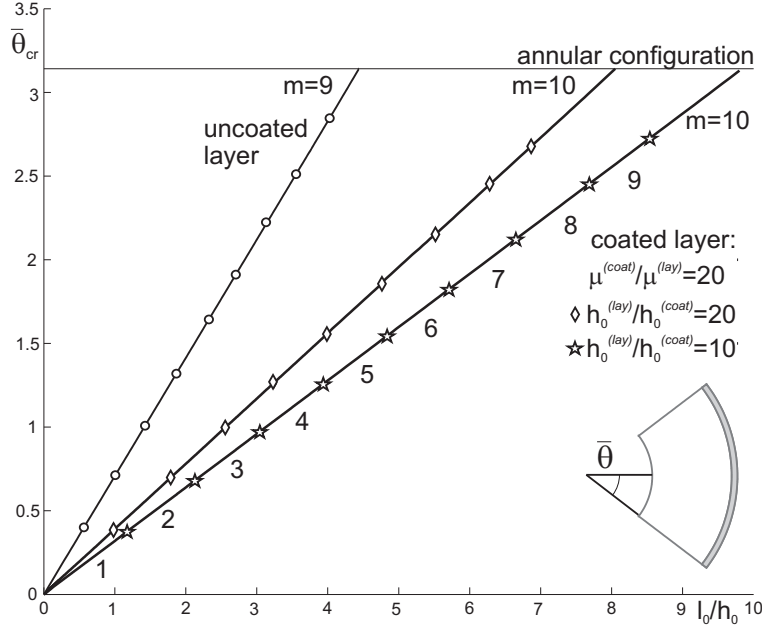


Figure 4.3: Comparison between the critical angle $\bar{\theta}_{cr}$ at bifurcation versus aspect ratio l_0/h_0 of two neo-Hookean coated bilayers subject to bending with coating at the tensile side with $\mu^{(coat)}/\mu^{(lay)} = 20$ and $h_0^{(lay)}/h_0^{(coat)} = 10$ and 20, respectively. In every curve, a small symbol denotes a transition between two different integer values of m (the parameter which sets the circumferential wavenumber). Bifurcation angles for a single, uncoated layer are also reported.

critical diffuse mode is very close to the surface instability when the coating is located at the tensile side of the specimen (Fig. 4.1), while the two thresholds become well separated in the other case, namely, when the coating is located at the compressive side (Fig. 4.2). This is because, in the latter, bifurcation takes place with a buckling-like mode in the coating, then occurring at a low axial stretch in the stiff layer. We can also observe from Fig. 4.1 (Fig. 4.2) that for $l_0/h_0 > 10$ (for $l_0/h_0 > 6$) the coated structures can be bent to the annular configuration without ‘encountering’ any instability.

reconciled, since for a single layer the surface instability and the instability in diffused modes are very close and may be taken to coincide in a first approximation.

4. IN-PLANE INCREMENTAL BIFURCATIONS

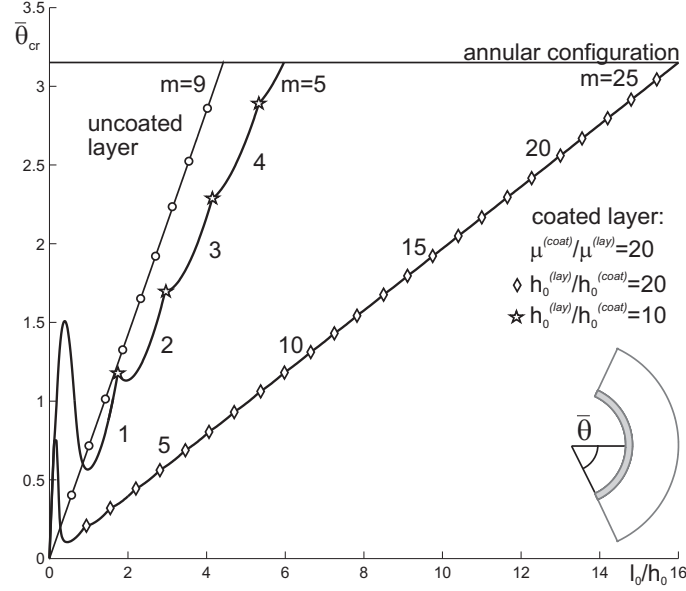


Figure 4.4: Comparison between the critical angle $\bar{\theta}_{cr}$ at bifurcation versus aspect ratio l_0/h_0 of two neo-Hookean coated bilayers subject to bending with coating at the compressed side with $\mu^{(coat)}/\mu^{(lay)} = 20$ and $h_0^{(lay)}/h_0^{(coat)} = 10$ and 20, respectively. In every curve, a small symbol denotes a transition between two different integer values of m (the parameter which sets the circumferential wavenumber). Bifurcation angles for a single, uncoated layer are also reported.

Some typical finite configurations and stress distributions at bifurcation corresponding to $l_0/h_0 = 2$ in Figs. 4.1 and 4.2 (indicated by small ‘square symbols’ on the bifurcation curve) are sketched in Fig. 3.2 for both positions of the stiff layer.

The critical angle at bifurcation is reported in Figs. 4.3 and 4.4 as a function of the aspect ratio l_0/h_0 for two values of coating thickness, $h_0^{(lay)}/h_0^{(coat)} = \{10, 20\}$ when the coating layer is on the tensile and on the compressive side, respectively. In the same figures the case of the uncoated layer is also reported for comparison. Note that results reported in Fig. 4.3 are similar to those reported in Fig. 6.1, since the coating is in the same

4.2 Bifurcation of a bilayer

position, though the stiffness ratio between coating and layer is different and equal to 20 in the former case and 500 in the latter. It is evident from the figures that the bifurcation solution for a single layer is approximated by a straight line, so that we can write down the approximated solution

$$\bar{\theta}_{cr} = 0.712 l_0/h_0, \quad (4.23)$$

which has passed unnoticed until the present work.

We may also notice that a linear relation between $\bar{\theta}_{cr}$ and l_0/h_0 is also evident in the cases of Figs. 6.1, 4.1, and 4.3, while such a linear relation holds only at high values of l_0/h_0 in the cases of Figs. 4.2 and 4.4. Moreover, the inclination of such lines depends on the elastic and thickness contrasts between layers, so that a simple formula like eqn. (4.23) is hard to be obtained.

Results for bifurcation of bent configurations for bilayers are presented in Figs. 4.5 and 4.6, in terms of critical semi-angle $\bar{\theta}_{cr}$ (upper part) and critical stretch at the compressed side of the specimen [$\lambda_{cr}(r_i^{(1)})$, lower part] as a function of the ‘global’ aspect ratio (the initial length divided by the initial total thickness). The ratios between the thicknesses and the shear coefficients μ_0 of the layers are (1 mm)/(5 mm) and (7 N/mm²)/(1 N/mm²) for Fig. 4.1, respectively, and (3 mm)/(40 mm) and (2.687 N/mm²)/(0.095 N/mm²) for Fig. 4.2. The various curves reported in Figs. 4.5 and 4.6 represent solutions corresponding to different bifurcation modes, singled out by the circumferential wavenumber m . The mode visible in an experiment is that corresponding to the lower value of the critical semi-angle, $\bar{\theta}_{cr}$, or to the higher value of critical stretch at the compressed side, λ_{cr} . Note that the gray zone represents the range of aspect ratios and bending semi-angle for which two neutral axes occur.

Within the set of aspect ratios and stiffness contrast analyzed in Fig. 4.5, a bifurcation only appears when two neutral axes have been formed, while it may occur when two or one neutral axes are present in Fig. 4.6. In all cases

4. IN-PLANE INCREMENTAL BIFURCATIONS

analyzed, including Figs. 4.5 and 4.6, we have found that the gray zone in the $\bar{\theta}_{cr}-l_0/h_0$ graphs is bounded by a straight line, becoming a horizontal line in the $\lambda_{cr}-l_0/h_0$ representation. The special feature emerging from Fig. 4.5 is that the mode $m=1$ of bifurcation becomes the critical mode for sufficiently high slenderness, so that here long-wavelength bifurcations (corresponding to small m) become well-separated from surface modes (corresponding to high m) and thus fully visible. This feature is also present in Fig. 4.6, which has been produced with values of parameters corresponding to commercially available rubbers (and tested by me, see Chapter 6). In this way it has been possible to produce the two samples shown in Figs. 6.6 and 6.8, differing only in the aspect ratio (taken equal to 2 for the sample shown in Fig. 6.6 and 1.5 for that shown in Fig. 6.8) and evidencing long-wavelength bifurcation modes.

We provide a justification of the finding that, when two neutral axes occur in a bilayer, the stretch (at the compressed side) is independent of the global aspect ratio l_0/h_0 , so that the gray zone (corresponding to the presence of two neutral axes) is bounded by a horizontal (inclined) line in the $\lambda_{cr}-l_0/h_0$ (in the $\bar{\theta}_{cr}-l_0/h_0$) representation, Figs. 4.5 and 4.6.

The explanation of this effect is based on two observations. (i.) During progressive bending of a bilayer with the stiff layer under compression, one neutral axis is present from the beginning of the bending within the soft layer, while the second neutral axis always nucleates at the interface between the two layers (and then moves in the stiff layer). (ii.) When the second neutral axis nucleates, the radial Cauchy stress T_r at the interface between layers takes a value independent of the initial aspect ratio l_0/h_0 . We can therefore operate on a single layer by imposing, in addition to the usual bending, a pressure P^{ext} at one of its external sides (of initial length l_0) to correspond to the radial stress at the interface between layers. In particular, we can apply P^{ext} at the side where the longitudinal stretch is greater than 1.

4.2 Bifurcation of a bilayer

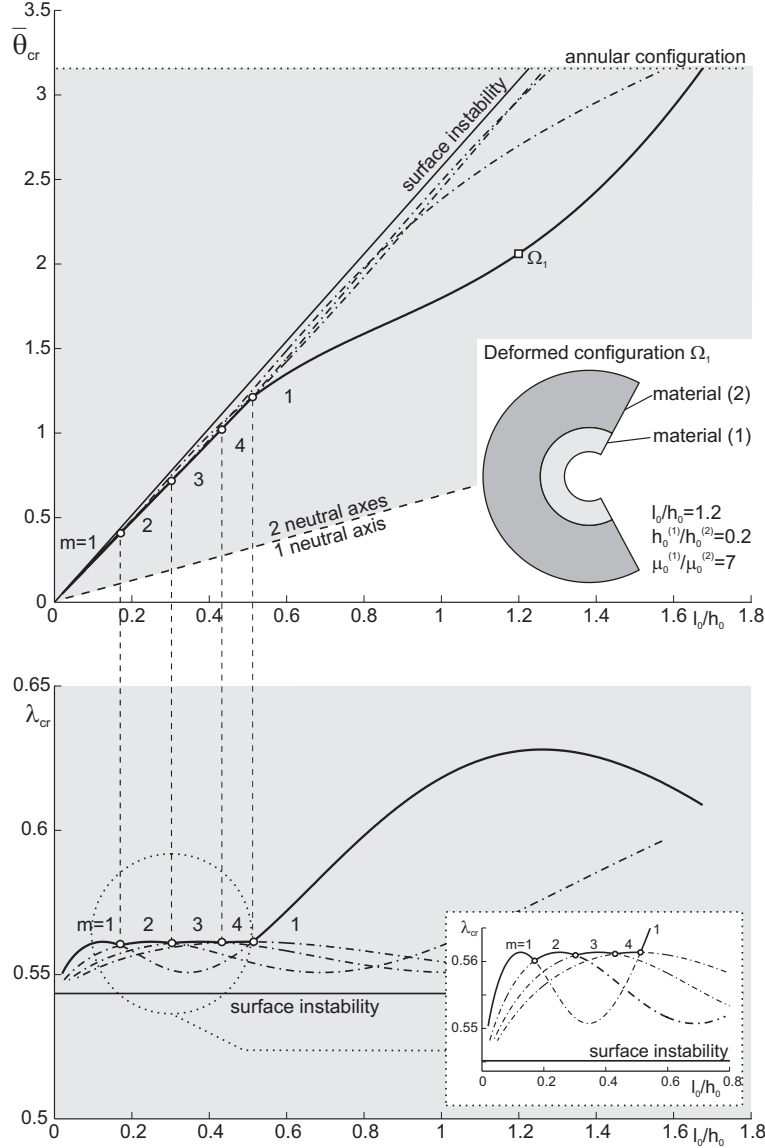


Figure 4.5: Critical angle $\bar{\theta}_{cr}$ and critical stretch λ_{cr} (evaluated at the internal boundary, $r = r_i^{(1)}$) versus aspect ratio l_0/h_0 for a Mooney-Rivlin bilayer coated with a stiff layer and subject to bending with $h_0^{(1)}/h_0^{(2)} = (1 \text{ mm})/(5 \text{ mm})$ and $\mu_0^{(1)}/\mu_0^{(2)} = (7 \text{ N/mm}^2)/(1 \text{ N/mm}^2)$. The stiff layer is located at the side in compression. In both plots, a small circle denotes a transition between two integer values of m (the parameter which sets the circumferential wavenumber). In the lower plot, the insert contains a magnification of the region where bifurcations occur at low l_0/h_0 . Two neutral axes occur in the region marked gray.

4. IN-PLANE INCREMENTAL BIFURCATIONS

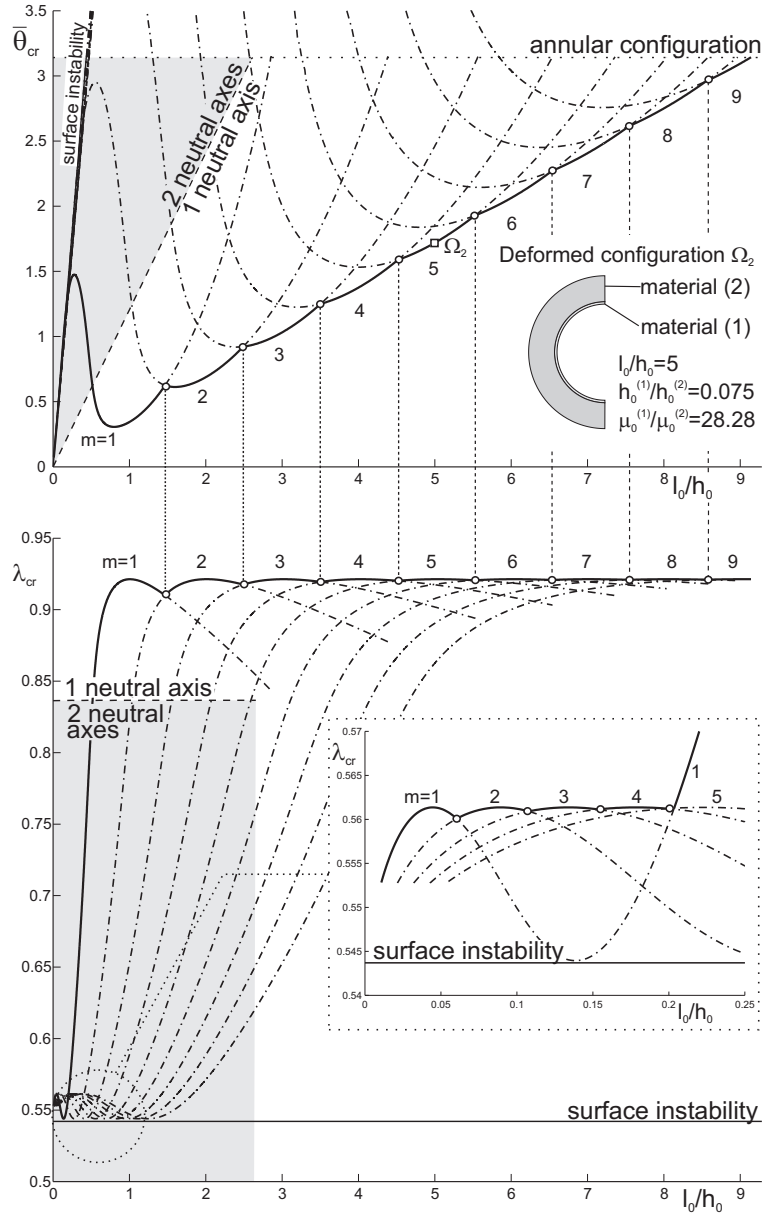


Figure 4.6: Critical angle $\bar{\theta}_{cr}$ and critical stretch λ_{cr} (evaluated at the internal boundary, $r = r_i^{(1)}$) versus aspect ratio l_0/h_0 for a Mooney-Rivlin bilayer coated with a stiff layer and subject to bending with $h_0^{(1)}/h_0^{(2)} = (3 \text{ mm})/(40 \text{ mm})$ and $\mu_0^{(1)}/\mu_0^{(2)} = (2.687 \text{ N/mm}^2)/(0.095 \text{ N/mm}^2)$. The stiff layer is located at the side in compression. In both plots, a small circle denotes a transition between two integer values of m (the parameter which sets the circumferential wavenumber). In the lower plot, the insert contains a magnification of the region where bifurcations occur at low l_0/h_0 . Two neutral axes occur in the region marked gray.

4.2 Bifurcation of a bilayer

To operate in dimensionless form, we introduce, from eqns. (3.9) and (3.13), the kinematic unknowns

$$\bar{\alpha} = \frac{2\bar{\theta}}{a}, \quad \bar{r} = \frac{r}{h_0}, \quad \bar{h} = \frac{h}{h_0}, \quad (4.24)$$

where $a = l_0/h_0$ is the aspect ratio of the undeformed configuration. The internal and external non-dimensional radii, from eqn. (3.3), are

$$\bar{r}_i = \frac{a}{2\bar{\theta}\bar{h}} - \frac{\bar{h}}{2}, \quad \bar{r}_e = \bar{r}_i + \bar{h}. \quad (4.25)$$

As we want to write the bending problem in terms of the variable $\lambda_i = \lambda(\bar{r}_i)$, we calculate $\bar{\theta}$ as a function of a , \bar{h} and λ_i , so that eqn. (3.13)₂ gives

$$\bar{\theta} = \frac{a}{\bar{h}} \left(\frac{1}{\bar{h}} - \lambda_i \right), \quad (4.26)$$

and the condition $\lambda_e = \lambda(\bar{r}_e)$ becomes

$$\lambda_e = \frac{2}{\bar{h}} - \lambda_i. \quad (4.27)$$

The boundary conditions for the layer under consideration are now

$$T_r(\bar{r}_i) = 0, \quad T_r(\bar{r}_e) = P^{ext}, \quad (4.28)$$

where

$$T_r = \frac{\mu_0}{2} \left(\lambda^2 + \frac{1}{\lambda^2} \right) + \gamma,$$

can be written from eqn. (3.16)₁. Eqn. (4.28)₂ provides the coefficient γ in the form

$$\gamma = P^{ext} - \frac{\mu_0}{2} \left(\lambda_e^2 + \frac{1}{\lambda_e^2} \right), \quad (4.29)$$

while, on the other hand, eqn. (4.28)₁ is equivalent to

$$\lambda_i^2 + \frac{1}{\lambda_i^2} + 2 \frac{P^{ext}}{\mu_0} - \left[\left(\frac{2}{\bar{h}} - \lambda_i \right)^2 + \left(\frac{2}{\bar{h}} - \lambda_i \right)^{-2} \right] = 0, \quad (4.30)$$

4. IN-PLANE INCREMENTAL BIFURCATIONS

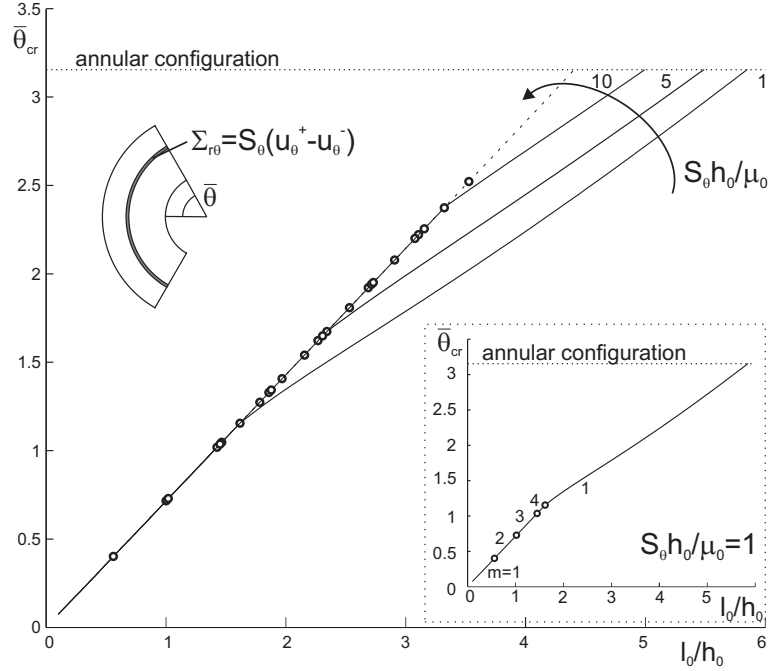


Figure 4.7: Critical angle $\bar{\theta}_{cr}$ at bifurcation versus the ‘global’ aspect ratio l_0/h_0 of two Mooney-Rivlin identical layers jointed through a ‘shear type’ imperfect interface. The dimensionless stiffness $S_\theta h_0/\mu_0$ takes the values 1, 5, and 10. The insert specifies the different values of m (the parameter which sets the circumferential wavenumber) at bifurcation for $S_\theta h_0/\mu_0 = 1$.

from which it is clear that the unknown \bar{h} is independent of a (but remains dependent on λ_i , μ_0 , and P^{ext}). Therefore, since a neutral axis corresponds to

$$T_\theta(\bar{r}_e) = 0, \quad (4.31)$$

eqns. (3.16)₂, (4.29), and (4.27) show that the neutral axis condition is independent of a , so that the solution in terms of λ_i becomes only a function of μ_0 and P^{ext} . The effects of an imperfect interface on bifurcations of a layered block under bending has never been analyzed, so that we limit the discussion to a simple situation, while a more detailed presentation will be the subject of future research. The simple example analyzed in Figs. 4.7

4.2 Bifurcation of a bilayer

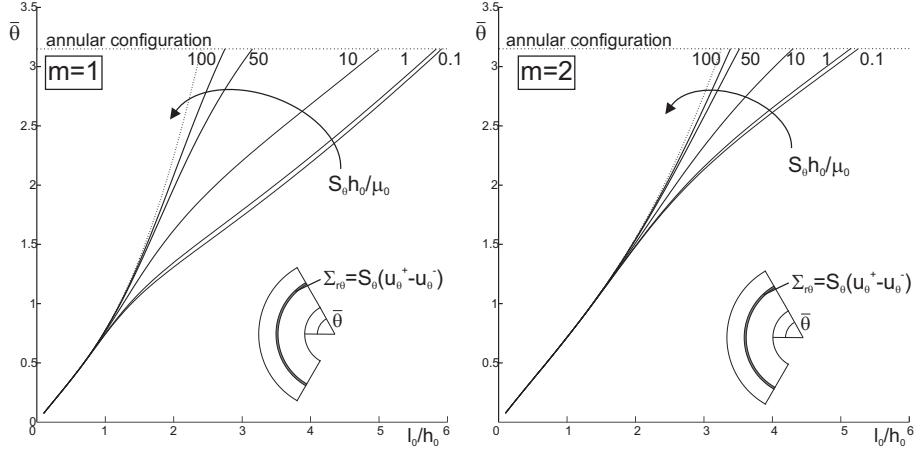


Figure 4.8: Bifurcation angles $\bar{\theta}$ at fixed circumferential number m versus the ‘global’ aspect ratio l_0/h_0 for two Mooney-Rivlin identical layers jointed through a ‘shear type’ imperfect interface as in Fig. 4.7. Left: $m=1$; right: $m=2$. A small number near a curve denotes the value of the dimensionless stiffness $S_\theta h_0/\mu_0$.

and 4.8 pertains to a uniform elastic block divided into two parts through an imperfect interface of dimensionless stiffness $S_\theta h_0/\mu_0$. Note that the interface is placed along the initial neutral axis. Results presented in Fig. 4.7 are in terms of the critical bending angle for bifurcation $\bar{\theta}_{cr}$, versus the initial ‘global’ aspect ratio l_0/h_0 , while similar results are reported in Fig. 4.8, but for a fixed circumferential wave number m . Therefore, $\bar{\theta}$ reported in Fig. 4.8 is not ‘critical’, in the sense that it is the bifurcation angle at fixed m , while $\bar{\theta}_{cr}$ is the smaller $\bar{\theta}$ for every m .

The results in Figs. 4.7 and 4.8 strongly depend on the dimensionless parameter $S_\theta h_0/\mu_0$ representing the interfacial stiffness, which yields an important decrease in the bifurcation angles with respect to the perfectly bonded case, which is approached at $S_\theta h_0/\mu_0 \rightarrow \infty$.

4. IN-PLANE INCREMENTAL BIFURCATIONS

5

Numerical procedures to determine the critical angle $\bar{\theta}_{cr}$ at bifurcation.

5.1 The determinantal method

The bifurcation condition can be numerically determined by introducing, for each layer, the vector

$$\mathbf{z}(r) = [f(r) \quad f'(r) \quad f''(r) \quad f'''(r)]^T, \quad (5.1)$$

so that the differential eqns. (4.13) can be rewritten as

$$\mathbf{z}' = \mathbf{N}\mathbf{z}, \quad (5.2)$$

where the matrix \mathbf{N} takes the form

$$\mathbf{N} = \begin{bmatrix} 0 & 1 & 0 & 0 \\ 0 & 0 & 1 & 0 \\ 0 & 0 & 0 & 1 \\ -N_{41} & -N_{42} & -N_{43} & -N_{44} \end{bmatrix}. \quad (5.3)$$

5. NUMERICAL PROCEDURES

Adopting the notation $\mathbf{X}_e^{(s)} = \mathbf{X}^{(s)}(r_e^{(s)})$ and $\mathbf{X}_i^{(s)} = \mathbf{X}^{(s)}(r_i^{(s)})$ for vectors or matrices referred to a generic layer s , and using eqns. (4.11)–(4.10), the continuity of incremental tractions and displacements at an interface between layers, eqns. (4.15), can be represented in matrix form as

$$\begin{bmatrix} \mathbf{Q}_e^{(s)} & -\mathbf{Q}_i^{(s+1)} \end{bmatrix} \begin{bmatrix} \mathbf{z}_e^{(s)} \\ \mathbf{z}_i^{(s+1)} \end{bmatrix} = \mathbf{0}, \quad (5.4)$$

where

$$\mathbf{Q}(r) = \begin{bmatrix} F(n^2 - 1) & r[F - n^2(2D + C - T_r)] & r^2(F + 3C) & r^3C \\ (n^2 - 1)(C - T_r) & r(C + T_r) & r^2C & 0 \\ 1 & 0 & 0 & 0 \\ 1 & r & 0 & 0 \end{bmatrix}, \quad (5.5)$$

while boundary conditions (4.20) can conveniently be rewritten as

$$\mathbf{P}_i^{(1)} \mathbf{z}_i^{(1)} = \mathbf{0}, \quad \mathbf{P}_e^{(N)} \mathbf{z}_e^{(N)} = \mathbf{0}, \quad (5.6)$$

where

$$\mathbf{P}(r) = \begin{bmatrix} F(n^2 - 1) & r[F - n^2(2D + C)] & r^2(F + 3C) & r^3C \\ n^2 - 1 & r & r^2 & 0 \end{bmatrix}. \quad (5.7)$$

We are now in a position to set the numerical solution procedure. Since in our examples we have always addressed systems with few layers, we use the simple following numerical procedure.

- 1) Employing a numerical integration based on an explicit Runge-Kutta (4,5)-formula, we solve, for each layer (index s has been dropped for simplicity), four initial-value problems. These are based on system (5.2), with the following four initial conditions:

$$\mathbf{z}_{(1)_i} = [1 \ 0 \ 0 \ 0]^T, \quad \mathbf{z}_{(2)_i} = [0 \ 1 \ 0 \ 0]^T,$$

5. NUMERICAL PROCEDURES

and

$$\hat{Q}_{i,e}^{(s)} = \begin{bmatrix} Q_{1j}^{(s)} z_{(1)j}^{(s)} & Q_{1j}^{(s)} z_{(2)j}^{(s)} & Q_{1j}^{(s)} z_{(3)j}^{(s)} & Q_{1j}^{(s)} z_{(4)j}^{(s)} \\ Q_{2j}^{(s)} z_{(1)j}^{(s)} & Q_{2j}^{(s)} z_{(2)j}^{(s)} & Q_{2j}^{(s)} z_{(3)j}^{(s)} & Q_{2j}^{(s)} z_{(4)j}^{(s)} \\ Q_{3j}^{(s)} z_{(1)j}^{(s)} & Q_{3j}^{(s)} z_{(2)j}^{(s)} & Q_{3j}^{(s)} z_{(3)j}^{(s)} & Q_{3j}^{(s)} z_{(4)j}^{(s)} \\ Q_{4j}^{(s)} z_{(1)j}^{(s)} & Q_{4j}^{(s)} z_{(2)j}^{(s)} & Q_{4j}^{(s)} z_{(3)j}^{(s)} & Q_{4j}^{(s)} z_{(4)j}^{(s)} \end{bmatrix}_{r=r_i, r_e}, \quad (5.13)$$

so that bifurcation corresponds to the condition that system (5.10) admits a non-trivial solution, namely,

$$\det \bar{\mathbf{W}} = 0, \quad (5.14)$$

which provides the critical semi-angle $\bar{\theta}_{cr}$.

5.2 The compound matrix method for a bilayer

The compound matrix method was initially proposed by Backus and Gilbert, Ref.[4], and applied to problems of fluid mechanics, Refs.[3, 36–38, 56], and solid mechanics, Refs. [32, 33]. Haughton and Orr, Ref. [29], used the method in incremental elasticity, while Refs. [18, 19, 22, 28] employed it to investigate instabilities of a homogeneous block subjected to finite flexure. Our aim is to show the application to elastic multilayers subject to finite bending in the simple case of a bilayer.

The differential equation (4.13) can be re-written as a linear system of first-order ODEs, that in the case of two elastic layers can be cast in the following standard form

$$\begin{aligned} \mathbf{y}' &= \mathbf{A}\mathbf{y}, \\ \mathbf{z}' &= \mathbf{B}\mathbf{z}, \end{aligned} \quad (5.15)$$

where vectors \mathbf{y} and \mathbf{z} are defined as

$$\begin{aligned} \mathbf{y}(r) &= [f^{(1)}(r) \quad (f^{(1)})'(r) \quad (f^{(1)})''(r) \quad (f^{(1)})'''(r)]^T, \\ \mathbf{z}(r) &= [f^{(2)}(r) \quad (f^{(2)})'(r) \quad (f^{(2)})''(r) \quad (f^{(2)})'''(r)]^T, \end{aligned} \quad (5.16)$$

5.2 The compound matrix method for a bilayer

and matrices \mathbf{A} and \mathbf{B} , which depend on the radial coordinate r , as

$$\mathbf{A}(r) = \begin{bmatrix} 0 & 1 & 0 & 0 \\ 0 & 0 & 1 & 0 \\ 0 & 0 & 0 & 1 \\ A_{41} & A_{42} & A_{43} & A_{44} \end{bmatrix}, \quad \mathbf{B}(r) = \begin{bmatrix} 0 & 1 & 0 & 0 \\ 0 & 0 & 1 & 0 \\ 0 & 0 & 0 & 1 \\ B_{41} & B_{42} & B_{43} & B_{44} \end{bmatrix}. \quad (5.17)$$

The components of \mathbf{A} and \mathbf{B} , as well as those of other matrices and vectors introduced in this Chapter are listed in Appendix A.

The boundary conditions at the two external surfaces of the layer, eqns. (4.20), are equivalent to

$$\mathbf{C}\mathbf{y}(r_i) = \mathbf{0}, \quad \mathbf{D}\mathbf{z}(r_e) = \mathbf{0}, \quad (5.18)$$

where $r_i = r_i^{(1)}$, $r_e = r_i^{(2)} + h^{(2)}$ and matrices \mathbf{C} and \mathbf{D} are

$$\mathbf{C} = \begin{bmatrix} C_{11} & C_{12} & C_{13} & C_{14} \\ C_{21} & C_{22} & C_{23} & 0 \end{bmatrix}, \quad \mathbf{D} = \begin{bmatrix} D_{11} & D_{12} & D_{13} & D_{14} \\ D_{21} & D_{22} & D_{23} & 0 \end{bmatrix}. \quad (5.19)$$

Continuity conditions between the two layers, eqns. (4.15), can be written as

$$\mathbf{G}\mathbf{y}(r_m) + \mathbf{H}\mathbf{z}(r_m) = \mathbf{0}, \quad (5.20)$$

where $r_m = r_i^{(1)} + h^{(1)}$ and matrices \mathbf{G} and \mathbf{H} are defined as

$$\mathbf{G} = \begin{bmatrix} G_{11} & G_{12} & G_{13} & G_{14} \\ G_{21} & G_{22} & G_{23} & 0 \\ G_{31} & 0 & 0 & 0 \\ G_{41} & G_{42} & 0 & 0 \end{bmatrix}, \quad \mathbf{H} = \begin{bmatrix} H_{11} & H_{12} & H_{13} & H_{14} \\ H_{21} & H_{22} & H_{23} & 0 \\ H_{31} & 0 & 0 & 0 \\ H_{41} & H_{42} & 0 & 0 \end{bmatrix}. \quad (5.21)$$

It is instrumental now to re-arrange the four solutions of eqns. (5.15): two for the first layer, \mathbf{y}^I , \mathbf{y}^{II} , and two for the second layer, \mathbf{z}^I , \mathbf{z}^{II} , [these solutions already satisfy the boundary conditions (5.18), but still not the

5. NUMERICAL PROCEDURES

interface conditions (5.21)] into two matrices sharing the following common structure

$$\begin{bmatrix} *^I_1 & *^{II}_1 \\ *^I_2 & *^{II}_2 \\ *^I_3 & *^{II}_3 \\ *^I_4 & *^{II}_4 \end{bmatrix}, \quad (5.22)$$

(where the symbol ‘*’ stands for either y or z) and defining the so-called ‘compound matrices’. Moreover, we introduce the vectors ϕ_i^y ($i = 1, \dots, 6$) and ϕ_i^z ($i = 1, \dots, 6$) collecting the components of the minors of matrices (5.22) as

$$\begin{aligned} \phi_1^* &= *^I_1 *^{II}_2 - *^I_2 *^{II}_1, & \phi_4^* &= *^I_2 *^{II}_3 - *^I_3 *^{II}_2, \\ \phi_2^* &= *^I_1 *^{II}_3 - *^I_3 *^{II}_1, & \phi_5^* &= *^I_2 *^{II}_4 - *^I_4 *^{II}_2, \\ \phi_3^* &= *^I_1 *^{II}_4 - *^I_4 *^{II}_1, & \phi_6^* &= *^I_3 *^{II}_4 - *^I_4 *^{II}_3. \end{aligned} \quad (5.23)$$

With the definitions (5.22) and (5.23), the differential problem (5.15) can be shown (Ref. [36]) to be equivalent to the new problem

$$(\phi^y)' = \mathbf{M}^A \phi^y, \quad (\phi^z)' = \mathbf{M}^B \phi^z, \quad (5.24)$$

where, introducing the symbol ‘ \square ’, equal to A (to B) for ϕ^y (for ϕ^z), we define

$$\mathbf{M}^\square = \begin{bmatrix} 0 & 1 & 0 & 0 & 0 & 0 \\ 0 & 0 & 1 & 1 & 0 & 0 \\ \square_{42} & \square_{43} & \square_{44} & 0 & 1 & 0 \\ 0 & 1 & 0 & 0 & 1 & 0 \\ -\square_{41} & 0 & 0 & \square_{43} & \square_{44} & 1 \\ 0 & -\square_{41} & 0 & -\square_{42} & 0 & \square_{44} \end{bmatrix}. \quad (5.25)$$

The system of differential eqns. (5.24) has to be solved using a Runge-Kutta (4,5) numerical method (we have used Matlab[®] ver. 7.9) to determine the vectors ϕ^y and ϕ^z .

5.2 The compound matrix method for a bilayer

The solution of the bifurcation problem can be written as a linear combination of the solutions \mathbf{y}^I , \mathbf{y}^{II} , \mathbf{z}^I , and \mathbf{z}^{II} ,

$$\begin{aligned}\mathbf{y} &= \xi_1 \mathbf{y}^I + \xi_2 \mathbf{y}^{II}, \\ \mathbf{z} &= \xi_3 \mathbf{z}^I + \xi_4 \mathbf{z}^{II},\end{aligned}\tag{5.26}$$

where the arbitrary coefficients ξ_i ($i = 1, \dots, 4$), which set the amplitude of the bifurcation mode, remain undefined in a linearized analysis. The conditions at the internal interface (5.20) can be recast as

$$\mathbf{W}\boldsymbol{\xi} = \mathbf{0}, \quad \text{with} \quad \boldsymbol{\xi} = [\xi_1 \ \xi_2 \ \xi_3 \ \xi_4]^T,\tag{5.27}$$

where

$$\mathbf{W} = \begin{bmatrix} \left(\mathbf{G}\mathbf{y}^I\right)_1 & \left(\mathbf{G}\mathbf{y}^{II}\right)_1 & \left(\mathbf{H}\mathbf{z}^I\right)_1 & \left(\mathbf{H}\mathbf{z}^{II}\right)_1 \\ \left(\mathbf{G}\mathbf{y}^I\right)_2 & \left(\mathbf{G}\mathbf{y}^{II}\right)_2 & \left(\mathbf{H}\mathbf{z}^I\right)_2 & \left(\mathbf{H}\mathbf{z}^{II}\right)_2 \\ \left(\mathbf{G}\mathbf{y}^I\right)_3 & \left(\mathbf{G}\mathbf{y}^{II}\right)_3 & \left(\mathbf{H}\mathbf{z}^I\right)_3 & \left(\mathbf{H}\mathbf{z}^{II}\right)_3 \\ \left(\mathbf{G}\mathbf{y}^I\right)_4 & \left(\mathbf{G}\mathbf{y}^{II}\right)_4 & \left(\mathbf{H}\mathbf{z}^I\right)_4 & \left(\mathbf{H}\mathbf{z}^{II}\right)_4 \end{bmatrix},\tag{5.28}$$

so that the bifurcation condition, depending on the bending semiangle $\bar{\theta}$, the undeformed aspect ratios l_0/h_0 and $h_0^{(1)}/h_0^{(2)}$, and the stiffness ratio $\mu_0^{(1)}/\mu_0^{(2)}$, becomes

$$\det(\mathbf{W}) = 0.\tag{5.29}$$

Condition (5.29) can be rewritten as the sum of 2×2 -determinants as

$$\begin{aligned} & \sum_{i=0}^1 (-1)^i \left\{ \begin{vmatrix} W_{1+i,1} & W_{1+i,2} \\ W_{41} & W_{42} \end{vmatrix} \begin{vmatrix} W_{2-i,3} & W_{2-i,4} \\ W_{33} & W_{34} \end{vmatrix} \right. \\ & - \begin{vmatrix} W_{2+i,1} & W_{2+i,2} \\ W_{11} & W_{12} \end{vmatrix} \begin{vmatrix} W_{3-i,3} & W_{3-i,4} \\ W_{43} & W_{44} \end{vmatrix} \\ & \left. - \begin{vmatrix} W_{2+2i,1} & W_{2+2i,2} \\ W_{31} & W_{32} \end{vmatrix} \begin{vmatrix} W_{4-2i,3} & W_{4-2i,4} \\ W_{13} & W_{14} \end{vmatrix} \right\} = 0. \end{aligned}\tag{5.30}$$

5. NUMERICAL PROCEDURES

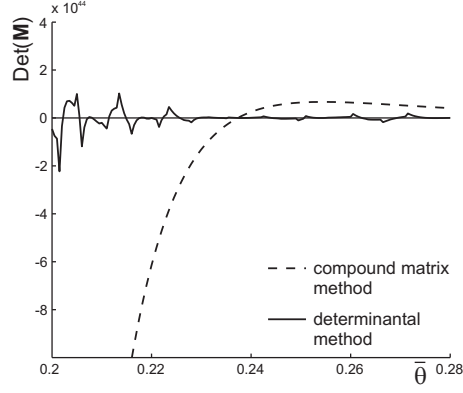


Figure 5.1: The compound matrix method (dashed line) against the determinantal method (solid line): $\det(\mathbf{M})$ is evaluated at different angles $\bar{\theta}$, for $l_0/h_0 = 0.1$, $h_0^{(1)}/h_0^{(2)} = (1 \text{ mm})/(5 \text{ mm})$ and $\mu_0^{(1)}/\mu_0^{(2)} = (7 \text{ N/mm}^2)/(1 \text{ N/mm}^2)$. Bifurcation corresponds to the vanishing of $\det(\mathbf{M})$; note the ‘spurious’ oscillations of the latter method.

The determinants can be expressed in terms of the vectors ϕ^y and ϕ^z as

$$\begin{aligned} \begin{vmatrix} W_{k1} & W_{k2} \\ W_{l1} & W_{l2} \end{vmatrix} &= (G_{k1}G_{l2} - G_{k2}G_{l1})\phi_1^y + (G_{k1}G_{l3} - G_{k3}G_{l1})\phi_2^y \\ &+ (G_{k1}G_{l4} - G_{k4}G_{l1})\phi_3^y + (G_{k2}G_{l3} - G_{k3}G_{l2})\phi_4^y \\ &+ (G_{k2}G_{l4} - G_{k4}G_{l2})\phi_5^y + (G_{k3}G_{l4} - G_{k4}G_{l3})\phi_6^y, \end{aligned} \quad (5.31)$$

and

$$\begin{aligned} \begin{vmatrix} W_{k3} & W_{k4} \\ W_{l3} & W_{l4} \end{vmatrix} &= (H_{k1}H_{l2} - H_{k2}H_{l1})\phi_1^z + (H_{k1}H_{l3} - H_{k3}H_{l1})\phi_2^z \\ &+ (H_{k1}H_{l4} - H_{k4}H_{l1})\phi_3^z + (H_{k2}H_{l3} - H_{k3}H_{l2})\phi_4^z \\ &+ (H_{k2}H_{l4} - H_{k4}H_{l2})\phi_5^z + (H_{k3}H_{l4} - H_{k4}H_{l3})\phi_6^z, \end{aligned} \quad (5.32)$$

in which indices k and l take the values corresponding to the representation (5.30). Once the undeformed aspect ratios l_0/h_0 and $h_0^{(1)}/h_0^{(2)}$ and the stiffness ratio $\mu_0^{(1)}/\mu_0^{(2)}$ have been fixed, the bifurcation condition (5.29), through

5.2 The compound matrix method for a bilayer

representation (5.30), becomes a function of the bending semiangle $\bar{\theta}$ only, to be solved numerically (we have used the function ‘fzero’ of Matlab[®] ver. 7.9). An example of the advantage related to the use of the compound matrix method over the ‘usual’ determinantal method is reported in Fig. 5.1, where $\det(\mathbf{W})$ is plotted as a function of $\bar{\theta}$ for a ‘stiff’ case, in which the superiority of the former approach is evident (note the ‘spurious’ oscillations of the determinantal method). In this particular case, the 2-norm condition number of the matrix \mathbf{W} is equal to 9.37×10^{27} , a value confirming that the matrix is bad conditioned.

5. NUMERICAL PROCEDURES

6

Experiments on coated and uncoated rubber blocks under bending

To substantiate the theoretical results on bifurcation of layered structures subject to finite bending, Roccabianca et al. (Refs. [43] and [44]) have designed and performed experiments, in the way initiated by Gent and Cho (Refs. [26] and [25]). In particular, we have imposed a finite bending to uncoated and coated elastic strips (made of natural rubber), employing the device shown in Fig. 6.2, in which a rubber strip is glued to two metallic platelets along the longer sides (using Loctite[®]) and these platelets are forced to impose a bending to the strip, using a simple screw-loading device. Two different coatings have been tested, both realized using 0.2 mm thick polyester transparent films (commercial copier films), glued singular or double (using Loctite[®]) to the rubber strip. During finite bending, the appearance of crazes has been detected by direct visual inspection.

The natural rubber and the polyester films (4 dog-bone shaped standard ISO 5277-1/1BA 30 mm × 5 mm samples for each material) have been tested under uniaxial stress, thus obtaining the results shown in Fig. 6.3,

6. EXPERIMENTS ON RUBBER BLOCKS

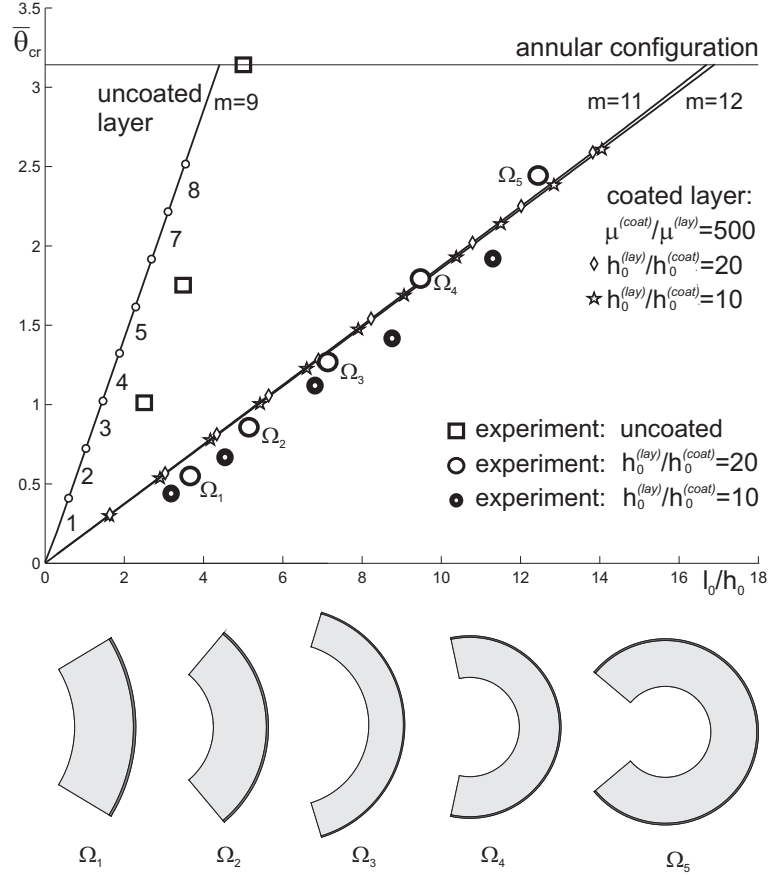


Figure 6.1: Experimental results versus theoretical predictions for the bifurcation opening semi-angle $\bar{\theta}_{cr}$ of uncoated and coated rubber strips subject to finite bending, versus the aspect ratio l_0/h_0 of the undeformed configuration. The shear moduli ratio $\mu^{(coat)}/\mu^{(lay)}$ of the coated layers has been taken equal to 500, while two thickness ratios $h_0^{(lay)}/h_0^{(coat)}$ equal to 20 and 10 have been considered. The critical theoretical configurations (for $h_0^{(lay)}/h_0^{(coat)} = 20$) corresponding to bifurcation points Ω_i ($i = 1, \dots, 4$) are sketched in the right part of the figure.

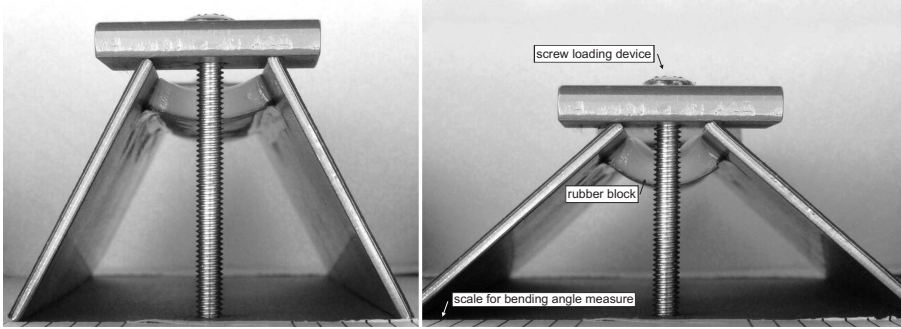


Figure 6.2: Device used to impose finite bending (of a semi-angle $\bar{\theta}$ equal to 25° on the left and to 45° on the right, with reference to Fig. 3.1) to coated and uncoated rubber strips (an uncoated $10\text{ mm} \times 100\text{ mm} \times 4\text{ mm}$ rubber strip is subject to bending in the photo).

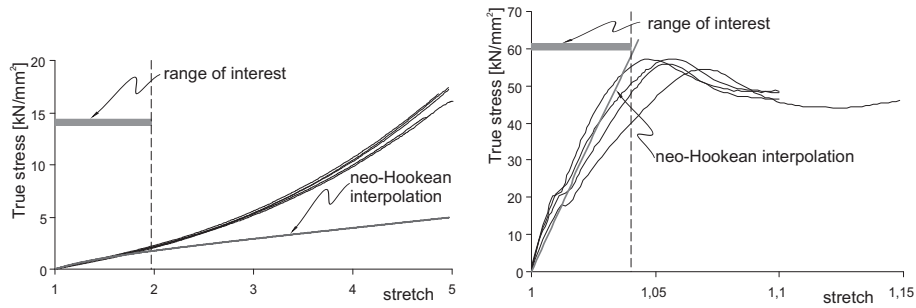


Figure 6.3: Uniaxial tests on and material characterizations of the natural rubber and the polyester film employed in the specimens. Note that the neo-Hookean interpolation has been selected to be valid only within the ‘range of interest’ to experimentally-detected bifurcations.

6. EXPERIMENTS ON RUBBER BLOCKS

where the true stress is plotted versus the stretch. It may be interesting to note that, while the response of the rubber is typical of these materials, the stress/stretch curve of the polyester film is highly nonlinear, exhibiting a peak and a softening regime. In the plots, the interpolation with the neo-Hookean material selected for the calculations is also included (giving $\mu^{(lay)} \simeq 1 \text{ kN/mm}^2$ and $\mu^{(coat)} \simeq 500 \text{ kN/mm}^2$). This interpolation curve may seem poor at a first glance, but we should point out that all the bifurcations found in the experiments have occurred with maximum stretches ranging between 1.52 and 1.9 (1.38 and 1.64 for samples with thick coating) in the rubber and between 1.02 and 1.04 (1.01 and 1.02 for samples with thick coating) in the polyester. For this reason, the selected neo-Hookean interpolation is much more accurate than it may appear and is taken valid either in tension or in compression. The progression of bending is shown in Fig. 6.4, referred to a $20 \text{ mm} \times 4 \text{ mm} \times 100 \text{ mm}$ rubber strip coated with two 0.2 mm thick films at the tensile side of the specimens (in which the larger dimension is that out-of-plane, taken sufficiently large to simulate the plane strain condition). At a certain stage of finite bending, namely at a certain bending semi-angle $\bar{\theta}_{cr}$, crazes can be detected to appear on the surface of the sample. This circumstance has been identified with appearance of small wavelength bifurcations¹ and compared with theoretical predictions for uncoated layers and for layer with a stiff coating at the tensile side of the specimen. Details of the surface of the block suffering compression are reported in Fig. 6.5 at different bending semi-angles (30° , 40° , 50°), from which we may note that crazes appear at an opening semi-angle lying between 30° and 40° . The results of experiments and theoretical predictions are summarized in Table 6.1, where bifurcation semi-angles are reported for

¹ Theoretical predictions indicate that the critical mode is always a diffuse mode, which –for obvious reasons– cannot be detected by direct visual inspection. However, for the geometries tested by us (an uncoated layer and layers coated at the side under tension) this mode is very close to a high-wavenumber mode, which is that detected by visual inspection.

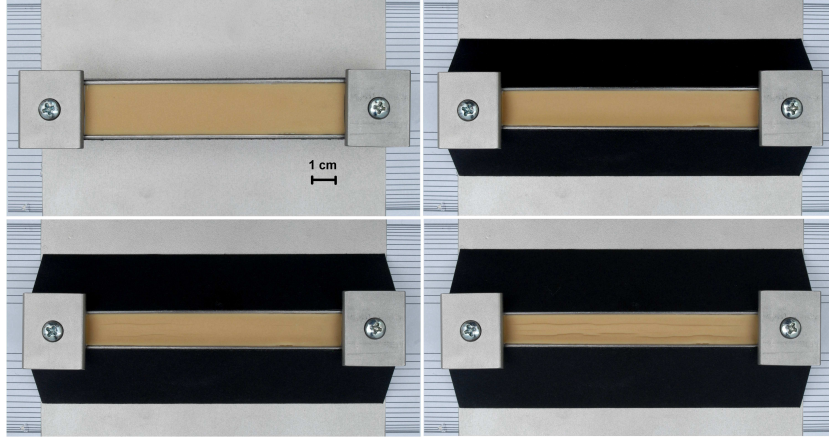


Figure 6.4: Finite bending of a $20 \text{ mm} \times 4 \text{ mm} \times 100 \text{ mm}$ rubber block coated with two polyester 0.2 mm thick films, imposed with the device shown in Fig. 6.2. From the top to the bottom, left to right: specimen before loading; specimen bent at a semi-angle of 30° (crazes are still not visible, see the detail reported in Fig. 6.5); specimen bent at a semi-angle of 40° (crazes become visible, see the detail reported in Fig. 6.5); specimen bent at a semi-angle of 50° (crazes invade the whole specimen, see the detail reported in Fig. 6.5).

the different geometries tested, and in Fig. 6.1. Despite the fact that our loading device does not exactly impose the correct boundary conditions on the planar sizes of the bent specimen (where the specimen should be free of sliding), the experimental results are in a fairly well agreement with the theoretical predictions (with a tendency toward overestimation of bifurcation angles) in all cases of uncoated and coated (two coating thicknesses, 0.2 and 0.4 mm , have been investigated) strips. In the second set of experiments to detect bifurcation, we have imposed finite bending to bi-layered systems made up of a natural rubber strip (3 mm thick) and a neoprene block (40 mm thick). In these case we have obtained only qualitative results. The bilayer is obtained by gluing the neoprene block to the natural rubber strip (we have used ethyl-cyanoacrylate, Pattex[®]), Fig. 6.6. Four dog-bone

6. EXPERIMENTS ON RUBBER BLOCKS

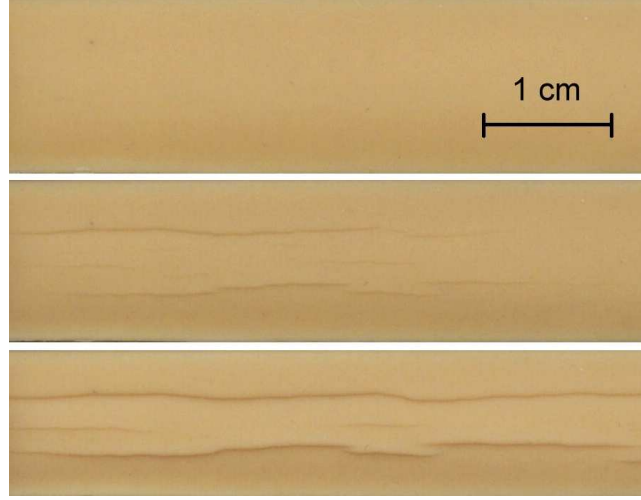


Figure 6.5: Details of Fig. 6.4. Crazes become visible in the photo taken at an opening semi-angle of 40° (centre) and invade the whole sample at 50° (lower part), while these remain undetected at 30° (upper part).

Table 6.1: Summary of experimental results (in terms of critical semi-angle at bifurcation, $\bar{\theta}_{cr}^{exp}$) and theoretical predictions ($\bar{\theta}_{cr}$) (the percentage error is denoted by ‘*err.*’) for rubber samples of thickness $h_0^{(lay)} = 4$ mm, uncoated and coated with a stiff 0.2 mm or 0.4 mm coating. $\bar{\theta}_{cr} = 180^\circ$ means that the annular configuration can be reached without bifurcation.

l_0 mm	$h_0^{(coat)} = 0$		$h_0^{(coat)} = 0.2$ mm			$h_0^{(coat)} = 0.4$ mm		
	$\bar{\theta}_{cr}^{exp}$	$(\bar{\theta}_{cr})$	$\bar{\theta}_{cr}^{exp}$	$(\bar{\theta}_{cr})$	<i>err.</i> [%]	$\bar{\theta}_{cr}^{exp}$	$(\bar{\theta}_{cr})$	<i>err.</i> [%]
10	58°	(101.99°)	–			–		
15	100°	(142.09°)	31°	(39.01°)	20.53	25°	(33.88°)	26.21
20	180°	(180°)	50°	(54.79°)	8.74	38°	(48.44°)	21.55
30	180°	(180°)	73°	(75.54°)	3.36	64°	(72.61°)	11.86
40	180°	(180°)	102°	(101.99°)	0.01	80°	(93.31°)	14.26
50	180°	(180°)	140°	(133.64°)	4.75	110°	(120.38°)	8.62

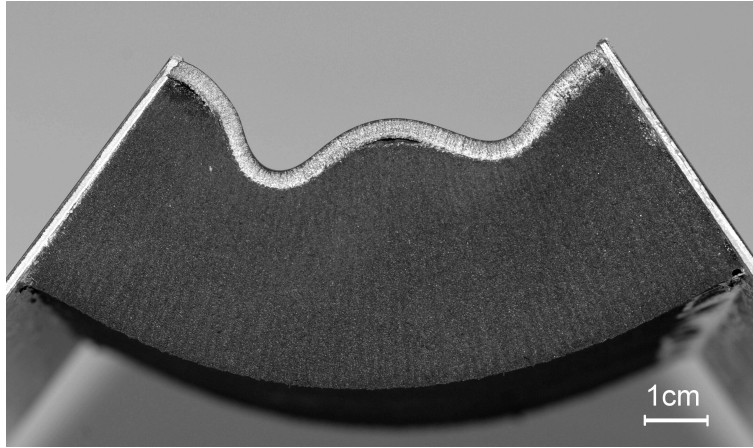


Figure 6.6: Bifurcation of a two-layer rubber block under finite bending evidencing long-wavelength bifurcation modes. Stiffness and thickness ratios between the layers are $(2.687 \text{ N/mm}^2)/(0.095 \text{ N/mm}^2)$ and $(3 \text{ mm})/(40 \text{ mm})$, respectively. The stiff layer ($86 \text{ mm} \times 3 \text{ mm} \times 150 \text{ mm}$, made up of natural rubber, marked with a white pencil on the sample) is at the compressive side and coats a neoprene layer ($86 \text{ mm} \times 40 \text{ mm} \times 150 \text{ mm}$).

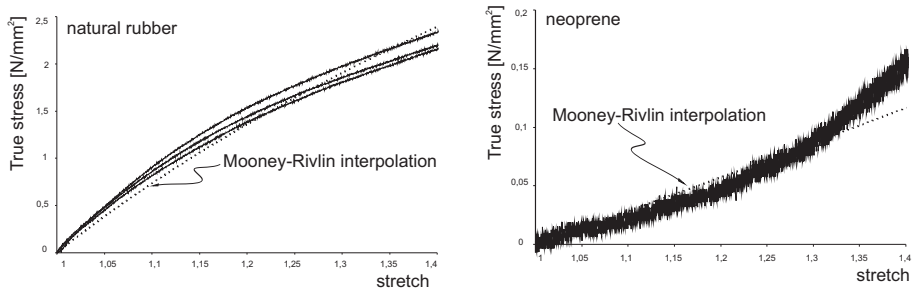


Figure 6.7: Uniaxial tests and material characterization of the natural rubber and the neoprene plate employed for the specimens to be subject to bending. Dotted curves represent Mooney-Rivlin interpolations employed in the analysis.

6. EXPERIMENTS ON RUBBER BLOCKS



Figure 6.8: Progressive bending of a two-layer rubber block (undeformed configuration is shown on the left, a bent configuration in the centre), evidencing bifurcation with long-wavelength bifurcation modes (shown on the right). Stiffness and thickness ratios between layers is $(2.687 \text{ N/mm}^2)/(0.095 \text{ N/mm}^2)$ and $(3 \text{ mm})/(40 \text{ mm})$, respectively. The stiff layer ($64.5 \text{ mm} \times 3 \text{ mm} \times 150 \text{ mm}$, made up of natural rubber, marked with a white pencil on the sample) is at the compressive side and coats a neoprene layer ($64.5 \text{ mm} \times 40 \text{ mm} \times 150 \text{ mm}$).

shaped standard ISO 5277-1/1BA $30 \text{ mm} \times 5 \text{ mm}$ specimens have been sampled from the two materials to characterize them in terms of Mooney-Rivlin model. Result of the tests (performed at room temperature with a Messphysik Midi 10 testing machine equipped with Doli Edc 222 acquisition and control electronics) are shown in Fig. 6.7, in terms of true stress versus stretch. The selected ranges of stress and stretch for the tests correspond to the values expected in the bending experiments. In the plots, the interpolation with the Mooney-Rivlin material (which provides a nearly-linear response at the stretch under consideration) selected for the calculations is also included. The least square method provides for the natural rubber $c_1^{(\text{natrub})} = 0.007 \text{ N/mm}^2$, $c_2^{(\text{natrub})} = 2.68 \text{ N/mm}^2$ (corresponding to $\mu_0^{(\text{natrub})} \simeq 2.687 \text{ N/mm}^2$) and for the neoprene $c_1^{(\text{neopr})} = 0.09 \text{ N/mm}^2$, $c_2^{(\text{neopr})} = 0.005 \text{ N/mm}^2$, giving $\mu_0^{(\text{neopr})} \simeq 0.095 \text{ N/mm}^2$. The progression of bending is shown in Fig. 6.8, referred to a $64.5 \text{ mm} \times 3 \text{ mm} \times 150 \text{ mm}$ rubber strip glued to a $64.5 \text{ mm} \times 40 \text{ mm} \times 150 \text{ mm}$ neoprene plate (in which the larger dimension is that out-of-plane, taken sufficiently large, 150 mm , to simulate the plane strain condition). At a certain stage of finite bending, namely at a certain bending semi-angle $\bar{\theta}_{cr}$, a long-wavelength mode can be

detected to appear on the surface of the sample (Fig. 6.8, right-hand side), which *qualitatively* confirms our findings.

From a quantitative point of view, the critical semi-angle for bifurcation results from modelling to be equal to 39.40° for the sample shown in Fig. 6.6 and 35.49° for that shown in Fig. 6.8, values that are definitely higher than those found experimentally (30° for the former sample and 21° for the latter). The fact that the theoretical predictions correspond to bifurcation angles larger than those observed experimentally is also common to all previous experiments Refs. [26, 44] and can be explained as the usual effect of imperfections (so that for instance the bending mode associated to the Euler buckling is always experimentally observed to become visible before the achievement of the critical load). The fact that the discrepancy between theoretical and experimental values is larger in the cases reported in the present article can be motivated in terms of the effect of the different *sensitivity* to imperfections. In fact, short-wavelength undulations introduced in the reference configuration start to amplify and to ‘become visible’ much closer to the bifurcation threshold than long-wavelength imperfections, a feature demonstrated through finite element numerical simulations performed with a commercial program Abaqus/CAE[®] ver.6.9. Plots of Fig. 6.9 have been evaluated with a stiffness and thickness ratios between layers equal to $(2.687 \text{ N/mm}^2)/(0.095 \text{ N/mm}^2)$ and $(3 \text{ mm})/(40 \text{ mm})$, respectively, which reproduce the tested sample shown on the right in Fig. 6.8 (undeformed global aspect ratio $l_0/h_0 = 1.5$). In the FEM analysis, a long-wavelength undulation with an amplitude of 0.2 mm has been introduced in the undeformed configuration (see Fig. 6.9, on the right) to simulate an initial imperfection.

6. EXPERIMENTS ON RUBBER BLOCKS

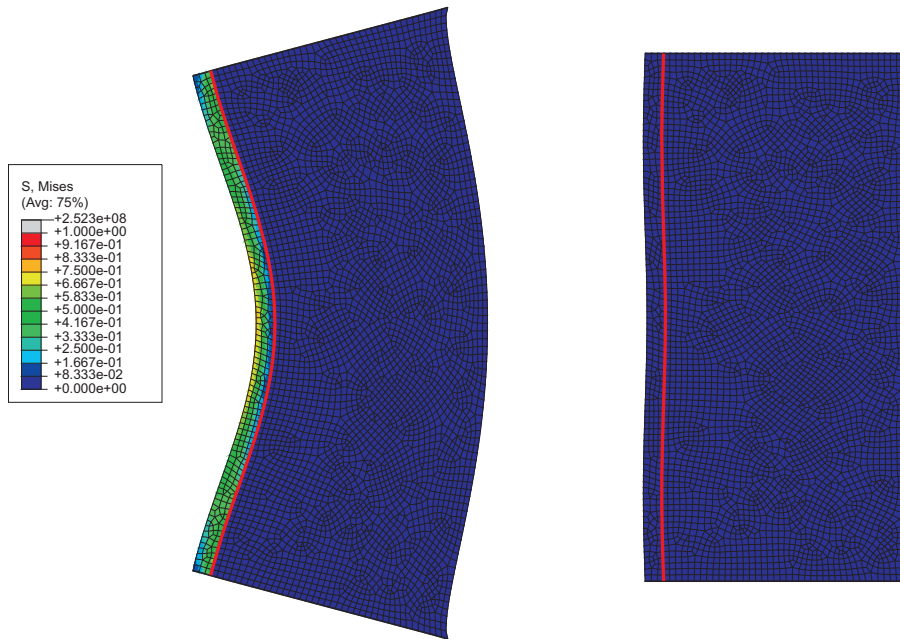


Figure 6.9: Finite element analysis of a bilayered block with stiffness and thickness ratios between the layers are $(2.687 \text{ N/mm}^2)/(0.095 \text{ N/mm}^2)$ and $(3 \text{ mm})/(40 \text{ mm})$, respectively. A red solid line represent the interface between layers.

7

Out-of-plane incremental bifurcations superimposed on finite bending of an elastic layered block

The goal of this section is to address the three-dimensional bifurcation problem of the multilayered body considered in Chapter 3 subjected to finite bending. The finite bending solution for a three-dimensional elastic layered block is similar to that described in Chapter 2.

7.1 General formulation

In this Chapter we analyze the out of plane bifurcation modes. In this framework in the reference stress-free configuration, denoting by \mathbf{e}_i^0 ($i = 1, 2, 3$) the common cartesian basis, the position of the generic point $\mathbf{x}^{0(s)}$ is given by

$$\mathbf{x}^{0(s)} = x_1^{0(s)} \mathbf{e}_1^0 + x_2^{0(s)} \mathbf{e}_2^0 + x_3^{0(s)} \mathbf{e}_3^0, \quad (7.1)$$

7. OUT-OF-PLANE INCREMENTAL BIFURCATIONS

with

$$x_1^{0(s)} \in [-h_0^{(s)}/2, h_0^{(s)}/2], \quad x_2^{0(s)} \in [-l_0/2, l_0/2], \quad x_3^{0(s)} \in (0, L), \quad (7.2)$$

where the difference from eqn. (3.2) is only in the definition of the domain for $x_3^{0(s)}$. Following the same approach, in the deformed configuration points of the s -th layer are transformed to points identified by

$$r^{(s)} \in [r_i^{(s)}, r_i^{(s)} + h^{(s)}], \quad \theta^{(s)} \in [-\bar{\theta}, +\bar{\theta}], \quad z^{(s)} \in (0, L),$$

as $\lambda_z = 1$, see eqn.(3.7).

We first analyse the incremental field equations for a single layer and then we formulate the complete problem adding the pertinent interface conditions between layers and external boundary conditions of the multilayered system. We refer to Chapter 2 for the notation. The gradient of incremental displacement $\mathbf{u}(\mathbf{x})$ is now given by

$$\begin{aligned} \mathbf{L} = & u_{r,r} \mathbf{e}_r \otimes \mathbf{e}_r + \frac{u_{r,\theta} - u_\theta}{r} \mathbf{e}_r \otimes \mathbf{e}_\theta + u_{r,z} \mathbf{e}_r \otimes \mathbf{e}_z + u_{\theta,r} \mathbf{e}_\theta \otimes \mathbf{e}_r \\ & + \frac{u_r + u_{\theta,\theta}}{r} \mathbf{e}_\theta \otimes \mathbf{e}_\theta + u_{\theta,z} \mathbf{e}_\theta \otimes \mathbf{e}_z + u_{z,r} \mathbf{e}_z \otimes \mathbf{e}_r + \frac{u_{z,\theta}}{r} \mathbf{e}_z \otimes \mathbf{e}_\theta + u_{z,z} \mathbf{e}_z \otimes \mathbf{e}_z, \end{aligned} \quad (7.3)$$

and the incompressibility condition ($\text{tr} \mathbf{L} = 0$) is

$$r u_{r,r} + u_r + u_{\theta,\theta} + r u_{z,z} = 0. \quad (7.4)$$

If the coordinate system of the current state is aligned to a principal directions of stress, the non-vanishing components of \mathbb{C} may be expressed as

$$\begin{aligned} C_{rrrr} &= 2\mu_1^* - T_r, & C_{\theta\theta\theta\theta} &= 2\mu_2^* - T_\theta, & C_{zzzz} &= 2\mu_3^* - T_z, \\ C_{r\theta r\theta} &= \mu_3 + \Gamma_3, & C_{r\theta\theta r} &= \mu_3 + p_3, & C_{\theta r\theta r} &= \mu_3 - \Gamma_3, \\ C_{r z r z} &= \mu_2 + \Gamma_2, & C_{r z z r} &= \mu_2 + p_2, & C_{z r z r} &= \mu_2 - \Gamma_2, \\ C_{\theta z \theta z} &= \mu_1 + \Gamma_1, & C_{\theta z z \theta} &= \mu_1 + p_1, & C_{z \theta z \theta} &= \mu_1 - \Gamma_1, \end{aligned} \quad (7.5)$$

7.1 General formulation

where

$$\begin{aligned}\Gamma_1 &= \frac{T_z - T_\theta}{2}, & \Gamma_2 &= \frac{T_z - T_r}{2}, & \Gamma_3 &= \frac{T_\theta - T_r}{2}, \\ p_1 &= -\frac{T_z + T_\theta}{2}, & p_2 &= -\frac{T_z + T_r}{2}, & p_3 &= -\frac{T_\theta + T_r}{2}.\end{aligned}\quad (7.6)$$

For a hyperelastic material the six independent moduli μ_i and μ_i^* ($i = 1, 2, 3$) (no sum on index) may be written as

$$\begin{aligned}2\mu_i^* &= \lambda_i \frac{\partial W}{\partial \lambda_i} + \lambda_i^2 \frac{\partial^2 W}{\partial \lambda_i^2} - \sum_{l \neq i} \lambda_i \lambda_l \frac{\partial^2 W}{\partial \lambda_i \partial \lambda_l} + \lambda_j \lambda_k \frac{\partial^2 W}{\partial \lambda_j \partial \lambda_k} \quad (j \neq k \neq i), \\ 2\mu_i &= (T_j - T_k) \frac{\lambda_j^2 + \lambda_k^2}{\lambda_j^2 - \lambda_k^2} \quad (j \neq k \neq i).\end{aligned}\quad (7.7)$$

The incremental constitutive equations in terms of the incremental first Piola-Kirchhoff stress tensor can be written as

$$\begin{aligned}\Sigma_{rr} &= -\dot{\pi} + (2\mu_1^* - T_r)u_{r,r}, \\ \Sigma_{\theta\theta} &= -\dot{\pi} + (2\mu_2^* - T_\theta) \frac{u_r + u_{\theta,\theta}}{r}, \\ \Sigma_{zz} &= -\dot{\pi} + (2\mu_3^* - T_z)u_{z,z}, \\ \Sigma_{r\theta} &= (\mu_3 + \Gamma_3) \frac{u_{r,\theta} - u_\theta}{r} + (\mu_3 + p_3)u_{\theta,r}, \\ \Sigma_{\theta r} &= (\mu_3 + p_3) \frac{u_{r,\theta} - u_\theta}{r} + (\mu_3 - \Gamma_3)u_{\theta,r}, \\ \Sigma_{rz} &= (\mu_2 + \Gamma_2)u_{r,z} + (\mu_2 + p_2)u_{z,r}, \\ \Sigma_{zr} &= (\mu_2 + p_2)u_{r,z} + (\mu_2 - \Gamma_2)u_{z,r}, \\ \Sigma_{\theta z} &= (\mu_1 + \Gamma_1)u_{\theta,z} + (\mu_1 + p_1) \frac{u_{z,\theta}}{r}, \\ \Sigma_{z\theta} &= (\mu_1 + p_1)u_{\theta,z} + (\mu_1 - \Gamma_1) \frac{u_{z,\theta}}{r},\end{aligned}\quad (7.8)$$

Consider the incremental equations of equilibrium, in polar coordinates,

$$\begin{aligned}\Sigma_{rr,r} + \frac{1}{r}\Sigma_{r\theta,\theta} + \Sigma_{rz,z} + \frac{\Sigma_{rr} - \Sigma_{\theta\theta}}{r} &= 0, \\ \Sigma_{\theta r,r} + \frac{1}{r}\Sigma_{\theta\theta,\theta} + \Sigma_{\theta z,z} + \frac{\Sigma_{\theta r} + \Sigma_{r\theta}}{r} &= 0, \\ \Sigma_{zr,r} + \frac{1}{r}\Sigma_{z\theta,\theta} + \Sigma_{zz,z} + \frac{\Sigma_{zr}}{r} &= 0,\end{aligned}\quad (7.9)$$

7. OUT-OF-PLANE INCREMENTAL BIFURCATIONS

so that a substitution of eqns. (7.8) in eqns.(7.9) provides

$$\begin{aligned}
 \dot{\pi}_{,r} &= \left\{ (2\mu_1^*)_{,r} + \frac{2\mu_1^* + p_3 - \Gamma_3}{r} \right\} u_{r,r} + (2\mu_1^* + p_3 + \Gamma_3)u_{r,rr} \\
 &\quad + (\mu_3 + \Gamma_3) \frac{u_{r,\theta\theta} - u_{\theta,\theta}}{r^2} + (\mu_3 + p_3) \frac{u_{\theta,r\theta}}{r} + (\mu_2 + \Gamma_2)u_{r,zz} \\
 &\quad + (\mu_2 + p_2)u_{z,rz} - (2\mu_2^+ + p_3 - \Gamma_3) \frac{u_r + u_{\theta,\theta}}{r}, \\
 \dot{\pi}_{,\theta} &= [r(\mu_3 - \Gamma_3)_{,r}] \left(u_{\theta,r} + \frac{u_{r,\theta} - u_\theta}{r} \right) + r(\mu_3 - \Gamma_3)u_{\theta,rr} \\
 &\quad + (\mu_3 + p_3)u_{r,\theta r} + (2\mu_2^* + p_3 - \Gamma_3) \frac{u_{r,\theta} + u_{\theta,\theta\theta}}{r} \\
 &\quad + r(\mu_1 + \Gamma_1)u_{\theta,zz} + (\mu_1 + p_1)u_{z,\theta z}, \\
 \dot{\pi}_{,z} &= [r(\mu_2 - \Gamma_2)_{,r}] \frac{u_{z,r}}{r} + [r(\mu_2 - p_2)_{,r}] \frac{u_{r,z}}{r} + r(\mu_2 - \Gamma_2)u_{z,rr} \\
 &\quad + (\mu_2 + p_2)u_{r,zr} + (2\mu_3^* + p_1 - \Gamma_1)u_{z,zz} + (\mu_1 - \Gamma_1) \frac{u_{z,\theta\theta}}{r} \\
 &\quad + (\mu_1 + p_1) \frac{u_{\theta,z\theta}}{r}.
 \end{aligned} \tag{7.10}$$

We seek bifurcations in the following separable variable form

$$\left\{ \begin{array}{l} u_r(r, \theta, z) = f(r) \cos n\theta \cos \eta z \\ u_\theta(r, \theta, z) = g(r) \sin n\theta \cos \eta z \\ u_z(r, \theta, z) = h(r) \cos n\theta \sin \eta z \\ \dot{\pi}(r, \theta, z) = k(r) \cos n\theta \cos \eta z \end{array} \right. , \tag{7.11}$$

where $f(r)$, $g(r)$, $h(r)$ and $k(r)$ are real functions and n is a real number to be determined by boundary conditions. Substitution of representations

7.1 General formulation

(7.11) in eqns. (7.10) yields

$$\begin{aligned}
k' &= \frac{f'}{r} \{2r(\mu_1^*)_{,r} + 2\mu_1^* - \mu_2 + \Gamma_1 + \Gamma_3\} + f''(2\mu_1^* - \mu_2 + \Gamma_2) \\
&\quad - \frac{f}{r^2} \{(\mu_3 + \Gamma_3)n^2 + (\mu_2 + \Gamma_2)r^2\eta^2 + 2\mu_2^* - \mu_2 - p_1 - p_3\} \\
&\quad - \frac{g'n}{r}(\mu_2 - \mu_3 - 2\mu_2^* - \Gamma_1) + \frac{gn}{r^2}(\mu_2 - \mu_3 - 2\mu_2^* - \Gamma_1), \\
nk &= f'(\mu_3 - \mu_1 + \Gamma_2) + \frac{f}{r}(2\mu_2^* - \mu_1 + \Gamma_1) - g'[r(\mu_3 + p_3)]_{,r} \\
&\quad + \frac{g}{r} \left\{ [r(\mu_3 - \Gamma_3)]_{,r} + r^2\eta^2(\mu_1 + \Gamma_1) + n^2(2\mu_2^* - \mu_1 + \Gamma_1) \right\} \\
\eta k &= \frac{f'''}{\eta}(\mu_2 - \Gamma_2) + \frac{f''}{r\eta} \{r(\mu_2 - \Gamma_2)_{,r} + 2(\mu_2 - \Gamma_2)\} \\
&\quad + f' \left\{ \frac{1}{r^2\eta} [r(\mu_2 - \Gamma_2)_{,r} - (\mu_2 - \Gamma_2) - n^2(\mu_1 - \Gamma_1)] \right. \\
&\quad \left. + \eta[\mu_2 - 2\mu_3^* + \Gamma_2] \right\} + f \left\{ \frac{1}{r^3\eta} [-r(\mu_2 - \Gamma_2)_{,r} - n^2(\mu_1 - \Gamma_1) \right. \\
&\quad \left. + \mu_2 - \Gamma_2] + \frac{\eta}{r} [r(\mu_2 + p_2)_{,r} + \mu_2 - 2\mu_3^* + \Gamma_2] \right\} + g'' \frac{n}{r\eta}(\mu_2 - \Gamma_2) \\
&\quad + g' \frac{n}{r^2\eta} \{r(\mu_2 - \Gamma_2)_{,r} - (\mu_2 - \Gamma_2)\} + g \left\{ \frac{n}{r^3\eta} [(\mu_2 - \Gamma_2) \right. \\
&\quad \left. - n^2(\mu_1 - \Gamma_1) - r(\mu_2 - \Gamma_2)_{,r}] + \frac{n\eta}{r} [\mu_1 - 2\mu_3^* + \Gamma_1] \right\}, \tag{7.12}
\end{aligned}$$

where a prime denotes differentiation with respect to r , note that the incompressibility condition

$$h = -\frac{(ng + f + rf')}{r\eta}, \tag{7.13}$$

has been employed to arrive at eqns. (7.12).

By differentiating eqns. (7.12)_{2,3} with respect to r and substituting in eqn. (7.12)₁, a system of two differential equations is obtained which defines the function $f(r)$, $g(r)$ within a generic layer. Once $f(r)$ and $g(r)$ are known, the other functions, $h(r)$ and $k(r)$, can be calculated by employing eqns.

7. OUT-OF-PLANE INCREMENTAL BIFURCATIONS

(7.12)₁ and (7.13)₂, respectively. The set of all functions $f^{(s)}(r)$, $g^{(s)}(r)$ and $(s = 1, \dots, N)$ can be obtained imposing continuity conditions at the interfaces and external boundary conditions.

Continuity of incremental tractions and displacements at interfaces can be represented as

$$\begin{aligned}
 u_r^{(s)} \Big|_{r=r_e^{(s)}} &= u_r^{(s+1)} \Big|_{r=r_i^{(s+1)}} , \\
 u_\theta^{(s)} \Big|_{r=r_e^{(s)}} &= u_\theta^{(s+1)} \Big|_{r=r_i^{(s+1)}} , \\
 u_z^{(s)} \Big|_{r=r_e^{(s)}} &= u_z^{(s+1)} \Big|_{r=r_i^{(s+1)}} , \\
 \Sigma_{rr}^{(s)} \Big|_{r=r_e^{(s)}} &= \Sigma_{rr}^{(s+1)} \Big|_{r=r_i^{(s+1)}} , \\
 \Sigma_{\theta r}^{(s)} \Big|_{r=r_e^{(s)}} &= \Sigma_{\theta r}^{(s+1)} \Big|_{r=r_i^{(s+1)}} , \\
 \Sigma_{zr}^{(s)} \Big|_{r=r_e^{(s)}} &= \Sigma_{zr}^{(s+1)} \Big|_{r=r_i^{(s+1)}} ,
 \end{aligned} \tag{7.14}$$

where $r_e^{(s)} = r_i^{(s)} + h^{(s)}$. For dead-load tractions on the external curved surfaces, the boundary conditions at $r = r_i^{(1)}$ and $r = r_e^{(N)}$ are

$$\Sigma_{rr}^{(1),(N)} \Big|_{r_i^{(1)}, r_e^{(N)}} = 0, \quad \Sigma_{\theta r}^{(1),(N)} \Big|_{r_i^{(1)}, r_e^{(N)}} = 0, \quad \Sigma_{zr}^{(1),(N)} \Big|_{r_i^{(1)}, r_e^{(N)}} = 0. \tag{7.15}$$

On the boundaries $\theta = \pm\bar{\theta}$ we require that shear stresses and incremental normal displacements vanish, namely

$$\Sigma_{r\theta}^{(s)} \Big|_{\theta=\pm\bar{\theta}} = 0, \quad u_\theta^{(s)} \Big|_{\theta=\pm\bar{\theta}} = 0, \tag{7.16}$$

a condition which is achieved if $\sin n\bar{\theta} = 0$ [see eqn. (??)] or, equivalently, using eqn. (3.10), if

$$n = \frac{2m\pi}{\alpha l_0} \quad (m \in \mathbb{N}). \tag{7.17}$$

To obtain the axial compression we can imagine that the plate is compressed between rigid, lubricated plates. The appropriate end conditions are then

$$\Sigma_{rz}^{(s)} \Big|_{z=0,L} = 0, \quad \Sigma_{\theta z}^{(s)} \Big|_{z=0,L} = 0, \quad u_z^{(s)} \Big|_{z=0,L} = 0. \tag{7.18}$$

7.1 General formulation

To ensure this we require

$$\sin \eta L = 0 \quad (7.19)$$

so $\eta = \kappa\pi/L$, for some integer κ .

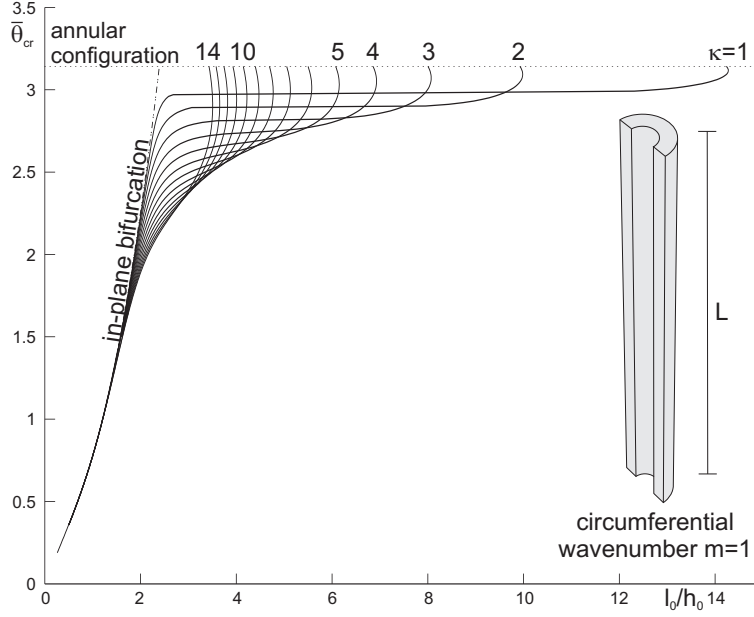


Figure 7.1: Plot of critical angle at bifurcation $\bar{\theta}_{cr}$ against aspect ratio l_0/h_0 (in-plane mode $m = 1$), for homogeneous plates of dimensionless height $L/h_0 = 50$. In each curve a small number denote the value of κ (the parameter which sets the out-of-plane wavenumber). The dash-dotted curve represent the in-plane bifurcation.

Since our goal is to employ a numerical method to evaluate the critical angle at bifurcation $\bar{\theta}_{cr}$, it becomes instrumental to rewrite eqns. (7.12) as a linear system of first-order ODEs. The procedure to derive numerically the bifurcation condition can be derived from the once described Chapter 5.

Eqns. (7.12) provide the critical angle at bifurcation ($\bar{\theta}_{cr}$) for a multi-layered elastic system subjected to bending in terms of initial aspect and stiffness ratios between layers. Once this angle is known, eqn. (3.13)₂ yields the critical stretch $\lambda_{cr} = 2\bar{\theta}_{cr}r_i^{(1)}/l_0$.

7. OUT-OF-PLANE INCREMENTAL BIFURCATIONS

7.2 Examples

7.2.1 The homogeneous block

The first example consists in the analysis of the three-dimensional bifurcations of a homogeneous, neo-Hookean elastic thick plate. This problem has been chosen as a benchmark but also to compare our results with those given by Haughton, Ref. [28]. In Fig. 7.1 the critical angle $\bar{\theta}_{cr}$ is reported as functions of the aspect ratio l_0/h_0 . Solid lines correspond to three-dimensional modes and numbers close to them denote parameter κ which, through eqn. (7.19), defines the out-of-plane wavenumber η . In Fig. 7.1 we are looking to circumferential mode $m = 1$, the dash-dotted line represent in-plane bifurcation corripondent to the same circumferential wavenumber. When the parameter κ is equal to 1 we have a bifurcation mode which can be compared with that of the Euler beam instability. In Fig. 7.2 the critical angle $\bar{\theta}_{cr}$ is reported as functions of the aspect ratio l_0/h_0 . The plots represent a plate of dimensionless height $L/h_0 = 50$ in the upper part of the figure, and with $L/h_0 = 10, 5$ in the lower part on the left and on the right, respectively. In addition in this plot however in-plane bifurcations (the lower boundary of gray regions corresponds to the occurence of an in-plane bifurcation modes) and surface instability threshold occurring at the compressed side (represented by a solid line in the plot) are also reported in order to determine the exact global behaviour of a solid block. It is important to observe that for values of the parameter m larger than one, the critical angle $\bar{\theta}_{cr}$ evaluated for in-plane and out-of-plane problems are very closed each other, so that the gray region is also very well bounded by the three-dimensional bifurcation curves for $m > 1$. It is clear that, for a plate with $L/h_0 = 50$, all blocks having $l_0/h_0 < 4.17$ loose uniqueness showing a prevalent plane-strain mode (almost independent of the z -direction), while for $4.17 < l_0/h_0 < 14.27$ three-dimensional modes play an important role. If we consider $L/h_0 = 10, 5$ as in the lower part of Fig. 7.2, we can see that

7.2 Examples

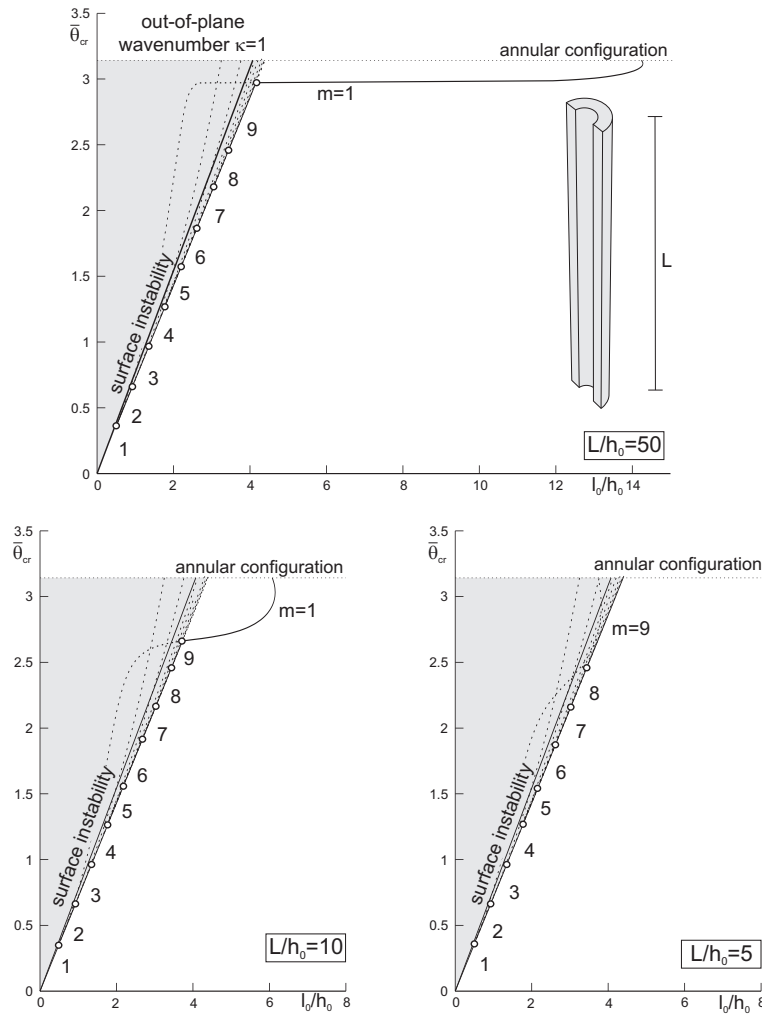


Figure 7.2: Plot of critical angle at bifurcation $\bar{\theta}_{cr}$ against aspect ratio l_0/h_0 (out-of-plane mode $\kappa = 1$) for plates of dimensionless height $L/h_0 = 50$ top position, and $L/h_0 = 10, 5$ bottom-left and bottom-right position, respectively. In each curve, a small circle denote a transition between two different integer values of m (the parameter which sets circumferential wavenumber). In the region marked gray the bifurcation is due to an in-plane mode. A solid line is used to plot the threshold of the surface instability.

the interval of aspect ratio in which the out-of-plane modes are important

7. OUT-OF-PLANE INCREMENTAL BIFURCATIONS

decreases, being equal to $3.72 < l_0/h_0 < 6.15$ on the left, or disappears, as it happens on the right. As a conclusion, we can state that for a bent plate the three-dimensional bifurcation investigation is important for slender specimens (high L/h_0) while for stub blocks (low L/h_0) the most restrictive limit is that obtained from a plane strain analysis.

7.2.2 A bilayered block

Although our analysis covers the case of a N -layer system, we will limit examples to the simple geometry of a two-layered system where, similarly to cases investigated in the previous Chapter, one of the layers is taken thin and rigid with respect to the other, so that it acts as a sort of stiff coating. Both layers are made up of neo-Hookean material.

The critical angle $\bar{\theta}_{cr}$ at bifurcation is reported in Fig. 7.3 as functions of the global aspect ratio l_0/h_0 (unloaded height of the specimen is l_0 and global thickness is h_0 , see Fig. 3.1), for a plate of dimensionless height $L/h_0 = 50$. The thickness and stiffness ratios used for the examples are $h_0^{(lay)}/h_0^{(coat)} = 10$ and $\mu^{(coat)}/\mu^{(lay)} = 20$, respectively. The difference between the upper and the lower part of the figure is that the coating layer is at the tensile side of the specimen in the former case, while it is at the compressive side in the latter. In the figures, bifurcation curves are reported for different values of the integer parameter κ which sets the wavenumber η in the z -direction. In Fig. 7.3 the circumferential wavenumber is set imposing the value of the parameter $m = 1$; in each plot a dash-dotted line represents the appropriate in-plane bifurcation correspondent to the same circumferential mode. We can see that, for an in-plane mode $m = 1$, the three-dimensional and the bidimensional analysis produce values of the critical angle at bifurcation very different (beyond $l_0/h_0 = 3.04$ in the upper plot and $l_0/h_0 = 1.64$ in the lower plot) and the out-of-plane bifurcation curves those setting the onset of the instability.

7.2 Examples

In Fig. 7.4 the critical angle $\bar{\theta}_{cr}$ is reported as functions of the aspect ratio l_0/h_0 . The plots represent a plate of dimensionless height $L/h_0 = 50$ on the left, and of dimensionless height $L/h_0 = 10$ on the right, respectively. The thickness and stiffness ratios used for these examples are $h_0^{(lay)}/h_0^{(coat)} = 10$ and $\mu^{(coat)}/\mu^{(lay)} = 20$. Again, in the upper part the coating is located at the tensile side while the coating is compressed in the lower part of the figure. Moreover, in these plots in-plane bifurcations (the lower boundary of gray regions corresponds to in-plane bifurcation modes) and the surface instability threshold occurring at the compressed side (represented by a solid line in the plot) are also reported. Bifurcation curves are reported for different values of the integer parameter m which, through eqn. (7.17), defines the circumferential wavenumber n . Obviously, for a given value of l_0/h_0 the bifurcation threshold is set by the value of m providing the minimum value of the critical angle. As in the case of a uniform block, for $m > 1$ the critical angle $\bar{\theta}_{cr}$ evaluated for in-plane and for out-of-plane problems are very closed each other, so that the gray region is also very well bounded by the three-dimensional bifurcations curves, independently of the position of the coating. As a partial conclusion, we can state that out-of-plane (3D) bifurcations are critical for slender plates (high values of L/h_0), while the in-plane analysis predicts the correct critical bending angle for relatively stub structures (low values of L/h_0).

To highlight the effect of the coating on the instability behaviour, we have produced Fig. 7.5 for the same geometries and mechanical properties. Solid lines represent the onset of bifurcation for the coated layers (copied from Fig. 7.4), while dashed curves set the critical configurations for the uncoated uniform block (see Fig. 7.2). We can appreciate that the presence of the coating changes strongly the behaviour of the block: if the coating is located at the tensile side $\bar{\theta}_{cr}$ decreases considerably, while if it is compressed the behaviour is more complex, inducing an increase of the bifurcation angle

7. OUT-OF-PLANE INCREMENTAL BIFURCATIONS

for low in-plane aspect ratios ($l_0/h_0 < 0.84$), the opposite for high values of l_0/h_0 .

7.2 Examples

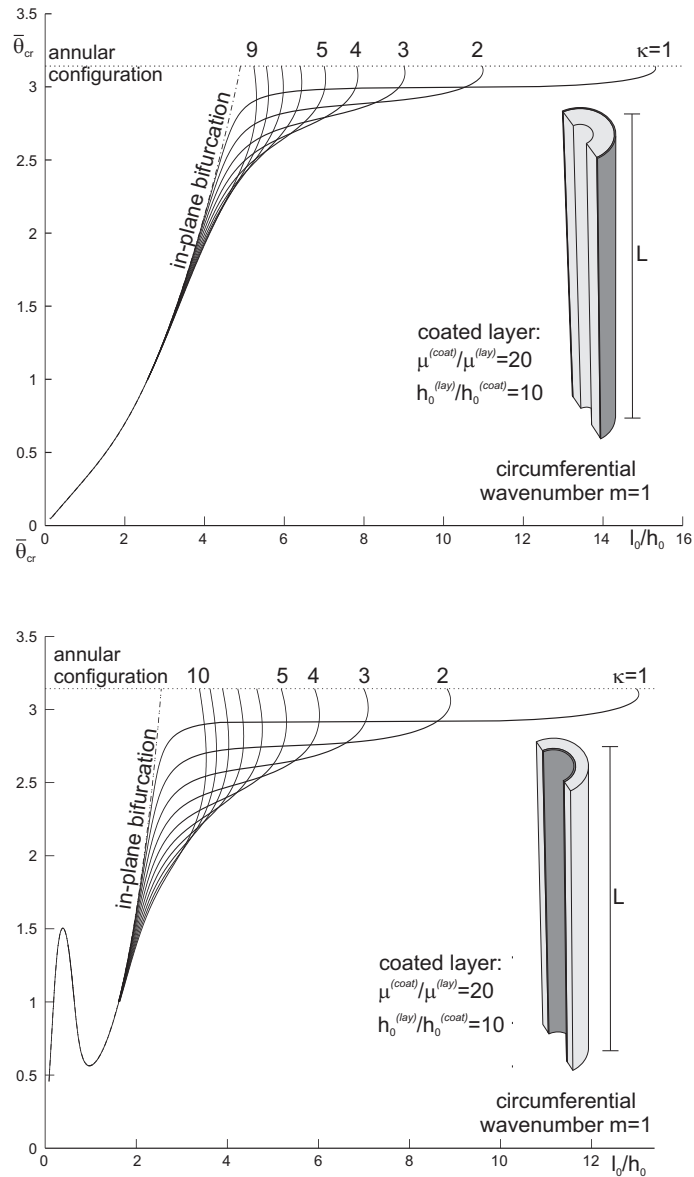


Figure 7.3: Plot of critical angle at bifurcation $\bar{\theta}_{cr}$ against global aspect ratio l_0/h_0 (in-plane mode $m = 1$), for plates of dimensionless height $L/h_0 = 50$ of a neo-Hookean coated bilayer subject to bending with $h_0^{(lay)}/h_0^{(coat)} = 10$ and $\mu^{(coat)}/\mu^{(lay)} = 20$. The coating is located at the tensile side in the upper part and at the compressed side in the lower part of the figure. In each curve a small number denote the value of κ (the parameter which sets the out-of-plane wavenumber). The dash-dotted curve represent the in-plane bifurcation.

7. OUT-OF-PLANE INCREMENTAL BIFURCATIONS

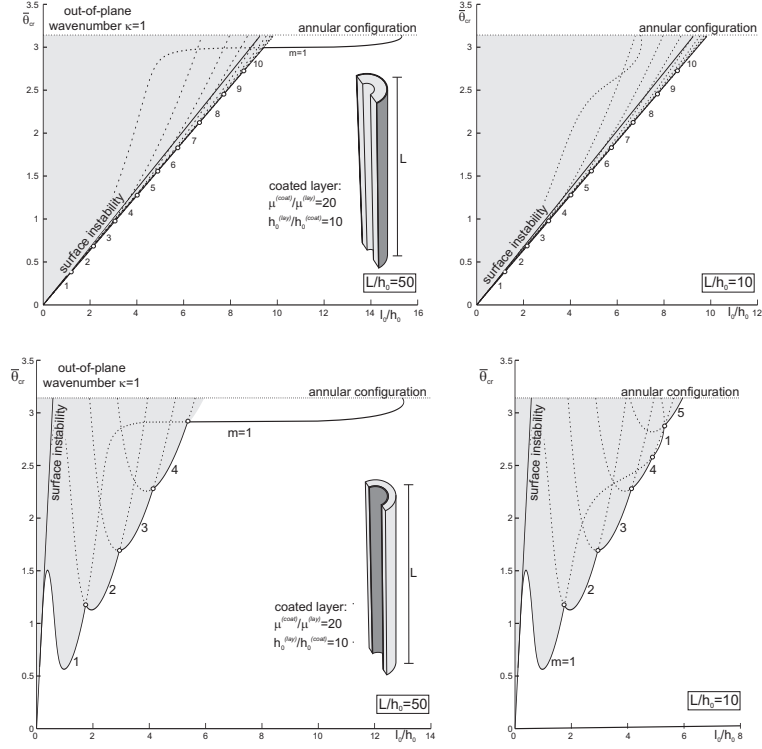


Figure 7.4: Plot of critical angle at bifurcation $\bar{\theta}_{cr}$ against global aspect ratio l_0/h_0 (out-of-plane mode $\kappa = 1$) for plates of dimensionless height $L/h_0 = 50, 10$ on the left and on the right, respectively. The bifurcation curves are evaluated for a coated bilayer with thickness and stiffness ratios $h_0^{(lay)}/h_0^{(coat)} = 10$ and $\mu^{(coat)}/\mu^{(lay)} = 20$. The coating is located at the tensile side in the upper part and at the compressed side in the lower part of the figure. In each curve, a small circle denote a transition between two different integer values of m (the parameter which sets circumferential wavenumber). In the region marked gray the bifurcation is due to an in-plane mode. A solid line is used to plot the threshold of the surface instability.

7.2 Examples

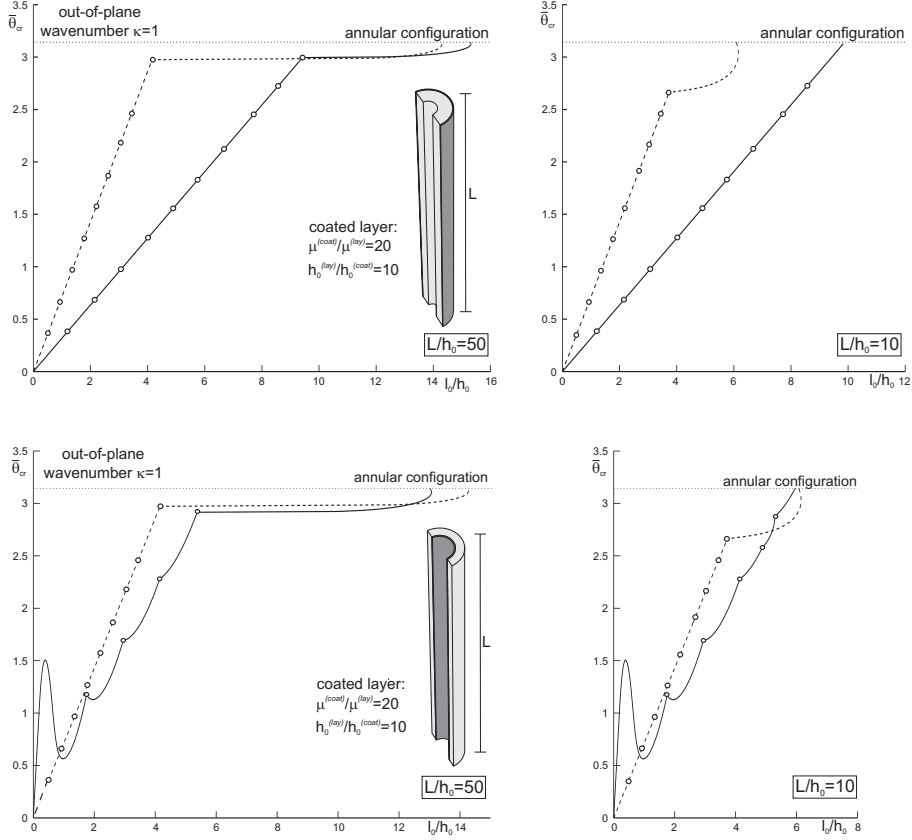


Figure 7.5: Plot of critical angle at bifurcation $\bar{\theta}_{cr}$ against global aspect ratio l_0/h_0 (out-of-plane mode $\kappa = 1$) for plates of dimensionless height $L/h_0 = 50, 10$ on the left and on the right, respectively. The bifurcation curves are evaluated for an homogenous block (dashes line) and for a coated bilayer (solid line) with thickness and stiffness ratios $h_0^{(lay)}/h_0^{(coat)} = 10$ and $\mu^{(coat)}/\mu^{(lay)} = 20$. The coating is located at the tensile side in the upper part and at the compressed side in the lower part of the figure. In each curve, a small circle denote a transition between two different integer values of m (the parameter which sets circumferential wavenumber).

7. OUT-OF-PLANE INCREMENTAL BIFURCATIONS

8

Conclusions

A new plane strain solution for finite bending of a thick, elastic multilayered plate has been studied, revealing the complex stress state developing in multilayered structures subject to large flexure, evidencing, for instance, more than one neutral axis. This solution allows treatment of two and three-dimensional bifurcations, highlighting the strong influence on critical configurations of geometry and stiffness contrast between layers. This analysis has been performed semi-analytically, developing, for the computation of the instability bending angles, a special application of a numerical method based on compound matrices, particularly well-performing for ‘stiff’ problems, as those where multiple neutral axes are present.

The case of coated plates has been considered in detail, investigating in-plane and three-dimensional instability modes. The following conclusions can be drawn:

- the presence of a stiff coating, both on the tensile or on the compressed sides, generally decreases the bifurcation bending angle;
- the occurrence of a critical diffuse mode is very close to the surface instability when the coating is located at the tensile side, while the two thresholds become well separated when the coating is located at the compressive side. This is because, in the latter, bifurcation takes place with a

8. CONCLUSIONS

buckling-like mode in the coating, then occurring at a low axial stretch in the stiff layer;

- the three-dimensional bifurcation analysis is significant only for relatively slender plates, independently of the position of the coating. In the other case, the plane strain investigation captures well the instability thresholds of the coated block.

The predictions of bifurcation configurations have been confirmed by performing simple experimental tests on rubber blocks coated by stiff layers, which give full evidence to short or long- wavelength modes depending on the considered specimen. It may be concluded that the theory can be effectively used to predict limits to the deformation capability of multilayered materials.

Appendix A

Matrices of numerical methods

$$\begin{aligned}O_{41}(r) &= (1 - n^2)(F - rF_{,r} - n^2E)/(Cr^4), \\O_{42}(r) &= [(rF + 2rn^2D)_{,r} - 2F]/(Cr^3), \\O_{43}(r) &= [(rF)_{,r} + 4F - 2n^2D]/(Cr^2), \\O_{44}(r) &= 2(F + 2C)/(Cr).\end{aligned}\tag{A.1}$$

$$\begin{aligned}A_{41}(r) &= (n^2 - 1)(F^{(1)} - rF_{,r}^{(1)} - n^2E^{(1)})/(C^{(1)}r^4), \\A_{42}(r) &= [2F^{(1)} - (rF^{(1)} + 2rn^2D^{(1)})_{,r}]/(C^{(1)}r^3), \\A_{43}(r) &= [2n^2D^{(1)} - (rF^{(1)})_{,r} - 4F^{(1)}]/(C^{(1)}r^2), \\A_{44}(r) &= -2(F^{(1)} + 2C^{(1)})/(C^{(1)}r).\end{aligned}\tag{A.2}$$

$$\begin{aligned}B_{41}(r) &= (n^2 - 1)(F^{(2)} - rF_{,r}^{(2)} - n^2E^{(2)})/(C^{(2)}r^4), \\B_{42}(r) &= [2F^{(2)} - (rF^{(2)} + 2rn^2D^{(2)})_{,r}]/(C^{(2)}r^3), \\B_{43}(r) &= [2n^2D^{(2)} - (rF^{(2)})_{,r} - 4F^{(2)}]/(C^{(2)}r^2), \\B_{44}(r) &= -2(F^{(2)} + 2C^{(2)})/(C^{(2)}r).\end{aligned}\tag{A.3}$$

A. MATRICES OF NUMERICAL METHODS

$$\begin{aligned}
C_{11} &= F^{(1)}(n^2 - 1), & D_{11} &= F^{(2)}(n^2 - 1), \\
C_{12} &= r_i[F^{(1)} - n^2(2D^{(1)} + C^{(1)})], & D_{12} &= r_e[F^{(2)} - n^2(2D^{(2)} + C^{(2)})], \\
C_{13} &= r_i^2(F^{(1)} + 3C^{(1)}), & D_{13} &= r_e^2(F^{(2)} + 3C^{(2)}), \\
C_{14} &= r_i^3C^{(1)}, & D_{14} &= r_e^3C^{(2)}, \\
C_{21} &= n^2 - 1, & D_{21} &= n^2 - 1, \\
C_{22} &= r_i, & D_{22} &= r_e, \\
C_{31} &= r_i^2, & D_{23} &= r_e^2.
\end{aligned} \tag{A.4}$$

$$\begin{aligned}
G_{11} &= F^{(1)}(n^2 - 1), & H_{11} &= F^{(2)}(1 - n^2), \\
G_{12} &= r_m[F^{(1)} - n^2(2D^{(1)} + C^{(1)} - T_r^{(1)})], & H_{12} &= r_m[n^2(2D^{(2)} + C^{(2)} - T_r^{(2)}) - F^{(2)}], \\
G_{13} &= r_m^2(F^{(1)} + 3C^{(1)}), & H_{13} &= -r_m^2(F^{(2)} + 3C^{(2)}), \\
G_{14} &= r_m^3C^{(1)}, & H_{14} &= -r_m^3C^{(2)}, \\
G_{21} &= (n^2 - 1)(C^{(1)} - T_r^{(1)}), & H_{21} &= (1 - n^2)(C^{(2)} - T_r^{(2)}), \\
G_{22} &= r_m(C^{(1)} + T_r^{(1)}), & H_{22} &= -r_m(C^{(2)} + T_r^{(2)}), \\
G_{23} &= r_m^2C^{(1)}, & H_{23} &= -r_m^2C^{(2)}, \\
G_{31} &= 1, & H_{31} &= -1, \\
G_{41} &= 1, & H_{41} &= -1, \\
G_{42} &= r_m, & H_{42} &= -r_m.
\end{aligned} \tag{A.5}$$

$$\begin{aligned}
P_{31}^A &= [2F^{(1)} - (rF^{(1)} + 2rn^2D^{(1)})_{,r}]/(C^{(1)}r^3), \\
P_{32}^A &= [2n^2D^{(1)} - (rF^{(1)})_{,r} - 4F^{(1)}]/(C^{(1)}r^2), \\
P_{33}^A &= -2(F^{(1)} + 2C^{(1)})/(C^{(1)}r), \\
P_{51}^A &= (1 - n^2)(F^{(1)} - rF_{,r}^{(1)} - n^2E^{(1)})/(C^{(1)}r^4), \\
P_{54}^A &= [2n^2D^{(1)} - (rF^{(1)})_{,r} - 4F^{(1)}]/(C^{(1)}r^2), \\
P_{55}^A &= -2(F^{(1)} + 2C^{(1)})/(C^{(1)}r), \\
P_{62}^A &= (1 - n^2)(F^{(1)} - rF_{,r}^{(1)} - n^2E^{(1)})/(C^{(1)}r^4), \\
P_{64}^A &= [(rF^{(1)} + 2rn^2D^{(1)})_{,r} - 2F^{(1)}]/(C^{(1)}r^3), \\
P_{66}^A &= -2(F^{(1)} + 2C^{(1)})/(C^{(1)}r).
\end{aligned} \tag{A.6}$$

$$\begin{aligned}
P_{31}^B &= [2F^{(2)} - (rF^{(2)} + 2rn^2D^{(2)})_{,r}]/(C^{(2)}r^3), \\
P_{32}^B &= [2n^2D^{(2)} - (rF^{(2)})_{,r} - 4F^{(2)}]/(C^{(2)}r^2), \\
P_{33}^B &= -2(F^{(2)} + 2C^{(2)})/(C^{(2)}r), \\
P_{51}^B &= (1 - n^2)(F^{(2)} - rF_{,r}^{(2)} - n^2E^{(2)})/(C^{(2)}r^4), \\
P_{54}^B &= [2n^2D^{(2)} - (rF^{(2)})_{,r} - 4F^{(2)}]/(C^{(2)}r^2), \\
P_{55}^B &= -2(F^{(2)} + 2C^{(2)})/(C^{(2)}r), \\
P_{62}^B &= (1 - n^2)(F^{(2)} - rF_{,r}^{(2)} - n^2E^{(2)})/(C^{(2)}r^4), \\
P_{64}^B &= [(rF^{(2)} + 2rn^2D^{(2)})_{,r} - 2F^{(2)}]/(C^{(2)}r^3), \\
P_{66}^B &= -2(F^{(2)} + 2C^{(2)})/(C^{(2)}r).
\end{aligned} \tag{A.7}$$

A. MATRICES OF NUMERICAL METHODS

References

- [1] M. Aaron and Y. Wang. Remarks concerning the flexure of a compressible nonlinearly elastic rectangular block. *J. Elasticity* , (40):99–106, 1995.
- [2] M. Aaron and Y. Wang. On deformations with constant modified stretches describing the bending of rectangular blocks. *Quart. Jl Mech. Appl. Math.* , (48):375–387, 1995.
- [3] N.R. Anturkar, T.C. Papanastasiou, and J.O. Wilkes. Compound matrix-method for eigenvalue problems in multiple connected domains. *Commun. Appl. Num. Meth.*, (8):811–818, 1992.
- [4] G.E. Backus and J.F. Gilbert. Numerical applications of a formalism for geophysical inverse problems. *Geophys. J. Roy. Astron. Soc.*, (13): 247–276, 1967.
- [5] A. Benallal, R. Billardon, and G. Geymonat. *Bifurcation and localization in rate-independent materials: some general considerations*. Number 327 in CISM Lecture Notes. Springer Berlin, 1993.
- [6] K. Bertoldi, D. Bigoni, and W. J. Drugan. Structural interfaces in linear elasticity. part i: Nonlocality and gradient approximations. *J. Mech. Phys. Solids* , (55):1–34, 2007.
- [7] D. Bigoni and M. Gei. Bifurcations of a coated, elastic cylinder. *Int. J. Solids Struct.* , (38):5117–5148, 2001.

REFERENCES

- [8] D. Bigoni and A. B. Movchan. Statics and dynamics of structural interfaces in elasticity. *Int. J. Solids Struct.* , (39):4843–4865, 2002.
- [9] D. Bigoni, M. Ortiz, and A. Needleman. Effect of interfacial compliance on bifurcation of a layer bonded to a substrate. *Int. J. Solids Struct.* , (34):4305–4326, 1997.
- [10] D. Bigoni, M. Gei, and S. Roccabianca. *Mathematical Methods and Models in Composites*, chapter Bifurcation of elastic multilayers. Mantic, V. (Ed). Imperial College Press, 2011.
- [11] M. A. Biot. *Mechanics of incremental deformations*. Wiley, New York, 1965.
- [12] O. Bruhns, H. Xiao, and A. Meyers. Finite bending of a rectangular block of an elastic hencky material. *J. Elasticity* , (66):237–256, 2002.
- [13] O. Bruhns, N. K. Gupta, A. T. M. Meyers, and H. Xiao. Bending of an elastoplastic strip with isotropic and kinematic hardening. *Arch. Appl. Mech.*, (72):759–778, 2003.
- [14] M. Brun, S. Guenneau, A. B. Movchan, and D. Bigoni. Dynamics of structural interfaces: Filtering and focussing effects for elastic waves. *J. Mech. Phys. Solids* , (58):1212–1224, 2010.
- [15] S.N.G. Chu. Elastic bending of semiconductor wafer revisited and comments on stoney’s equation. *J. Electrochem. Soc.*, (145):3621–3627, 1998.
- [16] T.J. Chuang and S. Lee. Elastic flexure of bilayered beams subjected to strain differentials. *J. Mater. Res.*, (15):2780–2788, 2000.
- [17] C. D. Coman and M. Destrade. Asymptotic results for bifurcation in pure bending of rubber blocks. *Quart. Jl Mech. Appl. Math.* , (61):395–414, 2008.

REFERENCES

- [18] M. Destrade, A. Ní Annaidh, and C.D. Coman. Bending instabilities of soft biological tissues. *Int. J. Solids Struct.* , (46):4322–4330, 2009.
- [19] M. Destrade, M.D. Gilchrist, J.A. Motherway, and J.G. Murphy. Bimodular rubber buckles early in bending. *Mech. Materials* , (42):469–476, 2010.
- [20] J. F. Dorris and S. Nemat-Nasser. Instability of a layer on a half space. *J. Appl. Mech.* , (47):304–312, 1980.
- [21] M. A. Dowdikh and R. W. Ogden. Interfacial waves and deformations in pre-stressed elastic media. *Proc. R. Soc. Lond. A*, (443):313–328, 1991.
- [22] G. Dryburgh and R. W. Ogden. Bifurcation of an elastic surface-coated incompressible isotropic elastic block subject to bending. *Z. angew. Math. Phys.* , (50):822–838, 1999.
- [23] Z. Fan, H. Razavi, J. Do, and A. et al. Morikawi. Three-dimensional nanopillar-array photovoltaics on low-cost and flexible substrates. *Nature Materials*, (8):648–653, 2009.
- [24] M. Gei and R. W. Ogden. Vibration of a surface-coated elastic block subject to bending. *Math. Mech. Solids* , (7):607–628, 2002.
- [25] A. N. Gent. Elastic instabilities in rubber. *Int. J. Non-linear Mech.* , (40):165–175, 2005.
- [26] A. N. Gent and I. S. Cho. Surface instabilities in compressed or bent rubber blocks. *Rubber Chem. Technol.* , (72):253–262, 1999.
- [27] A.E. Green and W. Zerna. *Theoretical Elasticity*. Oxford University Press, 1968.
- [28] D.M. Haughton. Flexure and compression of incompressible elastic plates. *Int. J. Engng. Sci.* , (37):1693–1708, 1999.

REFERENCES

- [29] D.M. Haughton and A. Orr. On the eversion of incompressible elastic cylinders. *Int. J. Non-linear Mech.* , (30):81–95, 1995.
- [30] R. Hill and J. W. Hutchinson. Bifurcation phenomena in the plane tension test. *J. Mech. Phys. Solids* , (23):239–264, 1975.
- [31] N. L’Heureux, N. Dusserre, G. Konig, B. Victor, P. Keire, T.N. Wight, and N.A.F. et al. Chronos. Human tissue-engineered blood vessel for adult arterial revascularization. *Nature Medicine*, (12):361–365, 2006.
- [32] K.A. Lindsay. The application of compound matrices to convection problems in multi-layered continua. *Math. Model. Method. Appl. Sci.*, (2):121–141, 1992.
- [33] K.A. Lindsay and C.E. Rooney. A note on compound matrices. *J. Comput. Phys.*, (103):472–477, 1992.
- [34] A.I. Lurie. *Theory of Elasticity*. Springer-Verlag, 2005.
- [35] A. Needleman. Non-normality and bifurcation in plane strain tension or compression. *J. Mech. Phys. Solids* , (27):231–254, 1979.
- [36] B.S. Ng and W.H. Reid. An initial value method for eigenvalue problems using compound matrices. *J. Comp. Phys.* , (30):125–136, 1979a.
- [37] B.S. Ng and W.H. Reid. A numerical method for linear two-point boundary-value problems using compound matrices. *J. Comp. Phys.* , (33):70–85, 1979b.
- [38] B.S. Ng and W.H. Reid. The compound matrix method for ordinary differential system. *J. Comp. Phys.* , (58):209–228, 1985.
- [39] R. W. Ogden. *Elastic deformations of rubberlike solids*. Mechanics of Solids, The Rodney Hill 60th Anniversary Volume. Pergamon Press, eds. h.g. hopkins and m.j. sewell edition, 1982.

REFERENCES

- [40] R. W. Ogden and D. A. Sotiropoulos. On interfacial waves in pre-stressed layered incompressible elastic solid. *Proc. R. Soc. Lond. A*, (450):319–341, 1995.
- [41] E. Papamichos, I. Vardoulakis, and H. B. Muhlhaus. Buckling of layered elastic media: a cosserat-continuum approach and its validation. *Int. J. Numer. Anal. Meth. Geomech.*, (14):473–498, 1990.
- [42] R. S. Rivlin. Large elastic deformations of isotropic materials. v. the problem of flexure. *Proc. R. Soc. Lond. A*, (195):463–473, 1949.
- [43] S. Roccabianca, M. Gei, and D. Bigoni. Plane strain bifurcations of elastic layered structures subject to finite bending: theory versus experiments. *IMA J. Appl. Math.*, (75):525–548, 2010.
- [44] S. Roccabianca, D. Bigoni, and M. Gei. Long wavelength bifurcations and multiple neutral axes of elastic layered structures subject to finite bending. *JOMMS*, 2011.
- [45] T. W. Shield, K. S. Kimand, and R. T. Shield. The buckling of an elastic layer bonded to an elastic substrate in plane strain. *J. Appl. Mech.*, (61):231–235, 1994.
- [46] P. S. Steif. Bimaterial interface instabilities in plastic solids. *Int. J. Solids Struct.*, (22):195–207, 1986.
- [47] P. S. Steif. Periodic necking instabilities in layered plastic solids. *Int. J. Solids Struct.*, (22):1571–1578, 1986.
- [48] P. S. Steif. An exact two-dimensional approach to fiber micro-buckling. *Int. J. Solids Struct.*, (23):1235–1246, 1987.
- [49] P. S. Steif. Interfacial instabilities in an unbounded layered solid. *Int. J. Solids Struct.*, (26):915–925, 1990.

REFERENCES

- [50] D. J. Steigmann and R. W. Ogden. Plane deformations of elastic solids with intrinsic boundary elasticity. *Proc. R. Soc. Lond. A*, (453):v, 1997.
- [51] Z. Suo, M. Ortiz, and A. Needleman. Stability of solids with interfaces. *J. Mech. Phys. Solids* , (40):613–640, 1992.
- [52] N. Triantafyllidis. Bifurcation phenomena in pure bending. *J. Mech. Phys. Solids* , (28):221–245, 1980.
- [53] N. Triantafyllidis and F. K. Lehner. Interfacial instability of density-stratified 2-layer systems under initial stress. *J. Mech. Phys. Solids* , (41):117–142, 1993.
- [54] N. Triantafyllidis and Y. M. Leroy. Stability of a frictional material layer resting on a viscous half-space. *J. Mech. Phys. Solids* , (42):51–110, 1994.
- [55] C. Truesdell and R.A. Toupin. *The Classical Field Theories*. In *Flügge, S., Ed., Encyclopedia of Physics*. Springer-Verlag, Berlin, 1960.
- [56] S.G. Yiantsios and B.G. Higgins. Numerical solution of eigenvalue problems using the compound matrix method. *J. Comp. Phys.* , (74):25–40, 1988.
- [57] N. J. B. Young. Bifurcation phenomena in the plane compression test. *J. Mech. Phys. Solids* , (24):77–91, 1976.